

Copyright
by
Phanisri Pradeep Pratapa
2011

The Thesis committee for Phanisri Pradeep Pratapa
Certifies that this is the approved version of the following thesis:

**Computational Simulation of Thunderstorm
Downbursts and Associated Wind Turbine Loads**

APPROVED BY

SUPERVISING COMMITTEE:

Supervisor: _____
Lance Manuel

Spyros A. Kinnas

**Computational Simulation of Thunderstorm
Downbursts and Associated Wind Turbine Loads**

by

Phanisri Pradeep Pratapa, B.Tech.

THESIS

Presented to the Faculty of the Graduate School of

The University of Texas at Austin

in Partial Fulfillment

of the Requirements

for the Degree of

Master of Science in Engineering

THE UNIVERSITY OF TEXAS AT AUSTIN

December 2011

Dedicated to my family.

Acknowledgments

I sincerely thank my supervisor Dr. Lance Manuel for giving me the opportunity to work on this project and for his guidance throughout the period. I also thank Dr. Spyros A. Kinnas of the Ocean Engineering Group at The University of Texas at Austin for imparting me with basic knowledge required for the project. His guidance and suggestions which helped in successful completion of this project are greatly acknowledged. I would also like to thank Mr. Hieu H. Nguyen, a Ph.D. student of Prof. Lance Manuel's research group. I acknowledge his patience and his suggestions from various informal discussions I had with him. I thank my fellow researchers and friends who have supported me throughout.

I thank my family for their support and unconditional love. My sincere gratitude to the Almighty with whose grace I am what I am today.

Computational Simulation of Thunderstorm Downbursts and Associated Wind Turbine Loads

Phanisri Pradeep Pratapa, M.S.E.
The University of Texas at Austin, 2011

Supervisor: Lance Manuel

Wind turbines operate in a constantly changing wind environment. This requires modeling and simulation of extreme events in which the wind turbine operates and a study of associated turbine loads as part of the design practice and/or site assessment. Thunderstorms are transient atmospheric events that occur frequently in some regions of the world and can influence the design of a wind turbine. Downbursts are extreme surface winds that are produced during a thunderstorm. They are both complex to model and their damaging effect on wind turbines has been noted in recent years. In the last few decades, downbursts have been the subject of studies in various fields—most notably, in aviation. Despite their complexity, generally only empirical models based on observational data have been developed for practical uses. Based on such field data as well as laboratory tests, it is common to model a downburst as a jet impingement on a flat plate. The actual buoyancy-driven flow has been commonly modeled as an equivalent momentum flux-driven flow

resulting from the impinging jet. The use of computational fluid dynamics (CFD) to model a downburst based on the idea of an impinging jet offers an alternative approach to experimental and analytical approaches.

Simulation of “downburst” wind fields using a computational model and analysis of associated loads on a wind turbine operating during such events is the subject of this study. Although downburst-like events have been simulated using commercial CFD software, the resulting wind fields from such simulations have not been used as inflow fields for wind turbine loads analysis. In this study, the commercial CFD software, ANSYS FLUENT 12.0, is used to simulate downburst events and the output wind fields are used as input to loads analysis for a utility-scale 5-MW wind turbine. The inflow wind fields are represented by both non-turbulent and turbulent components—the former are simulated using FLUENT while the latter are simulated as stochastic processes using Fourier techniques together with standard turbulence power spectral density functions and coherence functions. The CFD-based non-turbulent wind fields are compared with those from empirical/analytical approaches; turbine loads are also compared for the two approaches. The study suggests that a CFD-based approach can capture similar wind field characteristics as are modeled in the alternative approach; associated turbine loads are as well not noticeably different with the two approaches.

Table of Contents

Acknowledgments	v
Abstract	vi
List of Tables	x
List of Figures	xi
Chapter 1 Introduction	1
1.1 Background	1
1.2 Literature Review	3
1.3 Thesis Organization	5
Chapter 2 Development of Computational Model and Simulation of Downburst	7
2.1 Introduction	7
2.2 CFD-Based Wind Field Generation	8
2.2.1 Governing Equations	8
2.2.2 Reynolds Averaging	10
2.3 Computational Framework	13
2.3.1 Domain and Meshing	13
2.3.2 Solution Methodology	14
2.3.2.1 CFD Theory and Implementation	14
2.3.2.2 Implementation in FLUENT	15
2.3.3 Simulations	15
2.4 Model Development	15
2.4.1 Developing an application specific model	15
2.4.2 Description of the “non-turbulent” wind field	25
2.4.3 Solution convergence and choice of inlet velocity profile	25

2.4.4	Choice of grid and time step	27
2.5	The Paused Downburst Model	30
2.5.1	Time-independent model	30
2.5.2	Time-dependent model	37
2.5.3	Validation of the model	43
2.5.4	Limitations of the model	46
2.6	Generalized procedure to simulate downbursts using the “Paused Downburst” technique	47
2.7	Summary	52
Chapter 3 Response of a wind turbine subjected to the simu- lated downburst winds		54
3.1	Introduction	54
3.2	Wind field generation	55
3.2.1	Turbulence simulation	55
3.2.2	Wind field simulation using TurbSim	56
3.3	Wind Turbine Model	59
3.4	Wind Turbine Response analysis	60
3.5	Results and Discussion	60
3.6	Summary	62
Chapter 4 Conclusions		72
4.1	Overview of the research study	72
4.2	Concluding remarks	73
4.3	Recommendations for future work	73
Bibliography		75
Vita		79

List of Tables

2.1	Boundary conditions for the computational domain.	14
2.2	FLUENT Simulation parameters.	16
3.1	Values of the output and input parameters for the Paused Downburst model used for <i>Case1</i> and <i>Case2</i>	62
3.2	Downburst parameters used in the wind turbine loads analysis (for both <i>Case1</i> and <i>Case2</i>).	62

List of Figures

1.1 Schematic models of a downburst and a tornado (from Fujita [5]).	2
2.1 A representative sketch of the computational domain.	13
2.2 Wind speed record during the Andrews AFB microburst recorded on August 1, 1983 (from Fujita [5]).	17
2.3 Schematic model of an impinging jet showing different regions in the flow field.	19
2.4 Ring formation at the gust front of a downburst (from Fujita [5]).	20
2.5 Normalized radial velocity profiles for a Paused Downburst Model.	22
2.6 Velocity fields resulting from a steady-state simulation.	23
2.7 Velocity fields resulting from a paused snapshot of a simulation.	24
2.8 Grid dependency of solution with a uniform inlet velocity . . .	26
2.9 Inlet velocity profiles with zero velocity at interface	28
2.10 Grid dependency of solution with a parabolic inlet velocity profile	29
2.11 Tests for the choice of grid.	30
2.12 TTests for the choice of time step.	31
2.13 Computational domain used for the simulations.	32
2.14 Snapshot of a simulation at a paused instant.	33
2.15 Radial velocity distributions at the paused time instant (107 s).	35
2.16 Axial velocity distribution at the paused time instant (107 s).	36
2.17 Velocity distributions at the paused time instant (109 s) . . .	38
2.18 Velocity distributions at the paused time instant (113 s	38
2.19 Normalized peak radial velocity distributions.	41
2.20 Variation of $RMax$ with time.	42
2.21 Peak radial velocity distributions for the time-dependent model.	43
2.22 RRadial velocity profiles variation with height for the time-dependent Paused Downburst model.	44
2.23 Comparison of a wind speed time series resulting from the Paused Downburst model versus the Andrews AFB data.	46

2.24	Parameters in the generalized procedure to simulate a downburst using the Paused Downburst model.	48
2.25	Variation of $ZMax$ with tp^* : CHART-ZT.	50
2.26	Variation of $UrMax$ with tp^* : CHART-UT.	51
2.27	Variation of $RMax$ with tp^* : CHART-RT.	52
3.1	TurbSim simulation and its potential use in loads studies (Jonkman [8]). The coherent structures option is not employed in this study.	57
3.2	Flow field grid on the rotor plane of the wind turbine	58
3.3	Wind Turbine Model Information (from Jonkman et al. [9]).	59
3.4	Plan view of the downburst and the wind turbine (taken from Nguyen et al. [16]).	61
3.5	Comparison of wind speed (with turbulence) at hub height for <i>Case1</i>	63
3.6	Comparison of blade flap bending moment (with turbulence) for <i>Case1</i>	64
3.7	Comparison of wind speed (without turbulence) at hub height for <i>Case1</i>	65
3.8	Comparison of blade flap bending moment (without turbulence) for <i>Case1</i>	66
3.9	Comparison of wind speed (with turbulence) at hub height for <i>Case2</i>	67
3.10	Comparison of blade flap bending moment (with turbulence) for <i>Case2</i>	68
3.11	Comparison of wind speed (without turbulence) at hub height for <i>Case2</i>	69
3.12	Comparison of blade flap bending moment (without turbulence) for <i>Case2</i>	70

Chapter 1

Introduction

1.1 Background

Wind energy technology is rapidly developing and investment in wind energy is increasing worldwide. The cumulative wind power capacity of the United States is more than 40,000 MW, which constitutes about 3% of the overall power production in the country. Other countries such as China and India are also making rapid advances in wind power production. One could foresee large-scale investments in wind energy in the next few decades. This development can be accelerated if reliable and efficient design procedures can be established.

For tall structures such as wind turbines that are exposed to the environment, it is expected that large loads develop when these structures are subjected to extreme loading events. A thunderstorm is one such extreme event, similar to an earthquake or a hurricane, but more commonly occurring. A downburst is a phase in the evolution of a thunderstorm. Often, multiple downbursts can occur during a single thunderstorm. According to Fujita [5], a downburst is a sudden strong downdraft that induces an outburst of damaging winds at or near the ground. A downburst is further classified as a

macroburst or microburst depending on the spatial extent of the damaging winds. A macroburst has a spatial extent of more than 4 km; it usually lasts 5 to 30 minutes and causes maximum wind speeds up to around 60 m/s (134 mph). A microburst has a spatial extent of less than 4 km, with durations less than 10 minutes and maximum wind speeds up to around 75 m/s (168 mph). Although they are small in spatial extent and short-lived, intense microbursts can cause tornado-like damage. The winds diverge from a center in a downburst unlike in a tornado where they swirl, converge, and convect upwards (see Fig. 1.1).

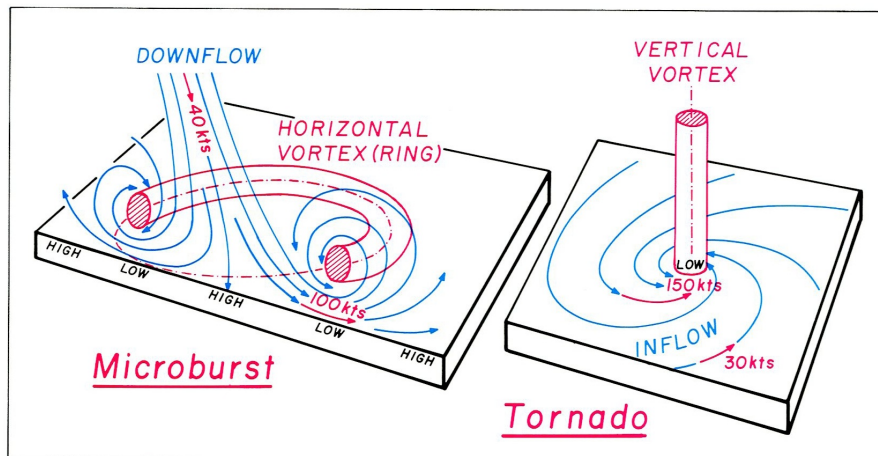


Figure 1.1: Schematic models of a downburst and a tornado (from Fujita [5]).

The driving mechanism behind a downdraft is natural convection and the development of a negative buoyancy situation. Lighter warm air convects upwards during a thunderstorm and gradually the water vapor in the air precipitates due to the normal lapse rate. While this occurs, the water vapor cools

the surrounding entrained air, thereby creating a negatively buoyant volume of air (Chay [3], Anabor et al. [2]). As this volume of air is of higher density, it is forced down towards the ground and, thus, causes a downdraft.

1.2 Literature Review

Researchers studying downbursts have come from the fields of atmospheric science as well as engineering. While some of them have made significant strides in simulating downbursts, while attempting to represent the physics behind the phenomenon, others have developed simpler models to facilitate their application in practice. The downburst mechanism and associated flow fields are complex phenomena to simulate. Depending on the end application, different approaches have been undertaken to characterize features of downburst-related wind fields.

As described earlier, a downburst is a buoyancy-driven flow. If one interprets the downburst phenomenon as a two-phase process, one phase that takes place prior the storm touchdown and the other after touchdown, the wind velocity profile in the latter phase has been found to have significant similarities with that of a radial wall jet (Hjelmfelt [7]). A radial wall jet is typically simulated as a jet impinging on a flat surface; this is essentially a momentum flux-driven flow. Downbursts are easier to simulate and study experimentally if they are thought to be represented as momentum flux-driven flow fields. A considerable amount of work has been done on impinging jets—both, experimentally (Wood et al. [25], Chay [3], Sengupta and Sarkar [21])

as well as computationally (Selvam and Holmes [19], Chay et al. [4], Kim and Hangan [11]). Experimental work on buoyancy-driven flow has been undertaken by Alahyari and Longmire [1] by releasing a high-density fluid into a low-density fluid.

Computational power and available resources in recent years have helped increase the use of CFD to simulate flow fields in complex problems. The earliest research studies on downbursts focused mainly on the steady-state solution of a jet impinging on a wall or plate. Later, features were added to represent actual characteristics of the downburst. A moving downburst that included transient features of an actual downburst was simulated by Sengupta et al. [20] and Li et al. [13]. Recently, Large-Eddy Simulation (LES) and Cloud models were developed (see, for example, Lin et al. [14], Anabor et al. [2]) to incorporate additional complex features of the downburst phenomenon.

With the help of extensive experimental studies that were undertaken, as well as with the help of computational simulations and available though limited downburst field data, attempts were made to develop simple analytical models to describe wind velocity profiles in downburst-like events. Although none of these available models include all the important features of an actual downburst, they offer reasonable representations of the event, albeit highly idealized. The analytical model developed by Oseguera and Bowles [17] and later improved by Vicroy [23] has been used by researchers (Chay et al. [4], Nguyen et al. [16]) for specific applications including wind turbine loads studies.

The present study is intended to complement the work of Nguyen et

al. [16], by developing a customized computational counterpart of the analytical model used in that cited study. Recognizing that the available models do not provide a complete representation of all the physical features of an actual downburst, the goal of this study is to develop a simulation model specific to an application (namely, a wind turbine loads study) by attempting to include storm physical characteristics that play a role in the wind field simulation. A “paused” downburst wind profile generated from such a physical CFD flow simulation is extracted as the non-turbulent wind profile to be used as part of the inflow wind field for aerodynamic loads calculation on a utility-scale 5-MW wind turbine.

1.3 Thesis Organization

The thesis is comprised of four chapters. The first chapter provided an overview of wind energy and the phenomenon of thunderstorm downbursts. It also discussed prior studies on downbursts and the context within which the model development of this study should be understood.

The second chapter presents the formulation and development of the computational model for downburst simulation that is intended for use in wind turbine loads studies. It describes various features of the model, its assumptions, and its limitations. Model validation against available downburst data is discussed.

The third chapter describes the wind turbine model used for the analysis, the generation of the 4-D wind fields, and the use of available wind turbine

load simulation software for analysis. It also compares turbine load results with other ongoing research that involves use of alternative downburst wind fields.

The concluding chapter summarizes this research study and presents observations and findings related this work.

Chapter 2

Development of Computational Model and Simulation of Downburst

2.1 Introduction

This chapter describes the use of computational fluid dynamics (CFD) to develop a model for thunderstorm downbursts. The mathematical formulation for any fluid dynamics problem involves a set of governing differential equations supported by initial and boundary conditions. These equations in continuous form are solved computationally by using appropriate spatial and temporal discretization. A difficulty in solution of such fluid dynamics problems lies in the modeling of turbulence of the flow. Turbulence, especially in the atmospheric boundary layer, is stochastic in nature and must be described by high Reynolds number flow regimes. Turbulence develops as an instability of laminar flow (Wilcox [24]). In the present study, turbulence in the inflow wind velocity field for wind turbine load simulation is dealt with in the conventional way by using stochastic Fourier-based simulation. This turbulent field is superimposed onto a mean or “non turbulent” velocity field (as in Chay et al. [4]); it is this mean wind field that is developed using CFD as described in this chapter.

2.2 CFD-Based Wind Field Generation

Although the commercial software, FLUENT, with built-in programs is used in the simulations, it is useful to present the governing equations and to gain an understanding of the theory underlying the wind field simulation.

2.2.1 Governing Equations

By idealizing a downburst as a jet impinging on a wall surface and assuming no temperature effects, the problem is mathematically represented by equations describing the conservation of mass (Eq. (2.1)) and the conservation of momentum (Eqs. (2.2), (2.3), and (2.4)). Also, we assume incompressible flow. Thus, we have:

$$\frac{\partial u}{\partial x} + \frac{\partial v}{\partial y} + \frac{\partial w}{\partial z} = 0 \quad (2.1)$$

$$\rho \frac{\partial u}{\partial t} + \rho u \frac{\partial u}{\partial x} + \rho v \frac{\partial u}{\partial y} + \rho w \frac{\partial u}{\partial z} = -\frac{\partial p}{\partial x} + \frac{\partial t_{11}}{\partial x} + \frac{\partial t_{21}}{\partial y} + \frac{\partial t_{31}}{\partial z} + \rho g_x \quad (2.2)$$

$$\rho \frac{\partial v}{\partial t} + \rho u \frac{\partial v}{\partial x} + \rho v \frac{\partial v}{\partial y} + \rho w \frac{\partial v}{\partial z} = -\frac{\partial p}{\partial y} + \frac{\partial t_{12}}{\partial x} + \frac{\partial t_{22}}{\partial y} + \frac{\partial t_{32}}{\partial z} + \rho g_y \quad (2.3)$$

$$\rho \frac{\partial w}{\partial t} + \rho u \frac{\partial w}{\partial x} + \rho v \frac{\partial w}{\partial y} + \rho w \frac{\partial w}{\partial z} = -\frac{\partial p}{\partial z} + \frac{\partial t_{13}}{\partial x} + \frac{\partial t_{23}}{\partial y} + \frac{\partial t_{33}}{\partial z} + \rho g_z \quad (2.4)$$

where u, v, w are components of velocity in the x, y, z Cartesian directions, respectively. Also, t refers to time, p is pressure, ρ is density, and g_x, g_y, g_z are components of the acceleration due to gravity in the three directions. The above equations are the Navier-Stokes equations.

The symmetric stress tensor is related to the strain-rate tensor as follows:

$$\begin{bmatrix} t_{11} & t_{12} & t_{13} \\ t_{21} & t_{22} & t_{23} \\ t_{31} & t_{32} & t_{33} \end{bmatrix} = \begin{bmatrix} 2\mu s_{11} & 2\mu s_{12} & 2\mu s_{13} \\ 2\mu s_{21} & 2\mu s_{22} & 2\mu s_{23} \\ 2\mu s_{31} & 2\mu s_{32} & 2\mu s_{33} \end{bmatrix} \quad (2.5)$$

where μ is the dynamic viscosity. The strain-rate tensor may be written as:

$$\begin{bmatrix} s_{11} & s_{12} & s_{13} \\ s_{21} & s_{22} & s_{23} \\ s_{31} & s_{32} & s_{33} \end{bmatrix} = \begin{bmatrix} \frac{\partial u}{\partial x} & \frac{1}{2} \left(\frac{\partial u}{\partial y} + \frac{\partial v}{\partial x} \right) & \frac{1}{2} \left(\frac{\partial u}{\partial z} + \frac{\partial w}{\partial x} \right) \\ \frac{1}{2} \left(\frac{\partial v}{\partial x} + \frac{\partial u}{\partial y} \right) & \frac{\partial v}{\partial y} & \frac{1}{2} \left(\frac{\partial v}{\partial z} + \frac{\partial w}{\partial y} \right) \\ \frac{1}{2} \left(\frac{\partial w}{\partial x} + \frac{\partial u}{\partial z} \right) & \frac{1}{2} \left(\frac{\partial w}{\partial y} + \frac{\partial v}{\partial z} \right) & \frac{\partial w}{\partial z} \end{bmatrix} \quad (2.6)$$

The Navier-Stokes equations cannot be solved analytically; computational solution is also not straightforward. To solve these equations with great accuracy, one could employ Direct Numerical Simulation (DNS) where all the spatial and temporal scales are fully resolved; this is a challenging task computationally. Another alternative is to use Large-Eddy Simulation (LES) where some scales of turbulence are resolved while others are modeled. Although LES requires less computational resources than DNS, a significant amount of computational resources are still necessary. A widely used approach (in CFD studies) is to solve the Navier-Stokes equations via statistical modeling where all the scales of turbulence are modeled. Such approaches uses Reynolds-Averaged Navier Stokes (RANS) equations along with a turbulence model.

2.2.2 Reynolds Averaging

In the Reynolds-Averaging approach, each physical entity (velocity component or pressure) is expressed as the sum of a mean (time-averaged) part and a fluctuating part. Thus, we have:

$$u(x, y, z, t) = U(x, y, z) + u'(x, y, z, t) \quad (2.7)$$

$$v(x, y, z, t) = V(x, y, z) + v'(x, y, z, t) \quad (2.8)$$

$$w(x, y, z, t) = W(x, y, z) + w'(x, y, z, t) \quad (2.9)$$

$$p(x, y, z, t) = P(x, y, z) + p'(x, y, z, t) \quad (2.10)$$

In Eqs. (2.7) to (2.10), U , V , W , and P may be termed “non-turbulent” components of u , v , w , and p respectively. An assumption made in the time averaging is that the turbulence is stationary.

By applying time averaging to the conservative form of Eqs. (2.1) to (2.4) and making use of Eq. (2.5), one obtains the Reynolds-Averaged Navier Stokes (RANS) equations (Eqs. (2.11) to (2.14)) where all the upper-case variables correspond to the mean component.

$$\frac{\partial U}{\partial x} + \frac{\partial V}{\partial y} + \frac{\partial W}{\partial z} = 0 \quad (2.11)$$

$$\begin{aligned} \rho \frac{\partial U}{\partial t} + \rho U \frac{\partial U}{\partial x} + \rho V \frac{\partial U}{\partial y} + \rho W \frac{\partial U}{\partial z} = & -\frac{\partial P}{\partial x} + \frac{\partial (2\mu S_{11} - \rho \overline{u'u'})}{\partial x} \\ & + \frac{\partial (2\mu S_{21} - \rho \overline{v'u'})}{\partial y} + \frac{\partial (2\mu S_{31} - \rho \overline{w'u'})}{\partial z} + \rho g_x \end{aligned} \quad (2.12)$$

$$\begin{aligned} \rho \frac{\partial V}{\partial t} + \rho U \frac{\partial V}{\partial x} + \rho V \frac{\partial V}{\partial y} + \rho W \frac{\partial V}{\partial z} = -\frac{\partial P}{\partial y} + \frac{\partial (2\mu S_{12} - \overline{\rho u'v'})}{\partial x} \\ + \frac{\partial (2\mu S_{22} - \overline{\rho v'v'})}{\partial y} + \frac{\partial (2\mu S_{32} - \overline{\rho w'v'})}{\partial z} + \rho g_y \end{aligned} \quad (2.13)$$

$$\begin{aligned} \rho \frac{\partial W}{\partial t} + \rho U \frac{\partial W}{\partial x} + \rho V \frac{\partial W}{\partial y} + \rho W \frac{\partial W}{\partial z} = -\frac{\partial P}{\partial z} + \frac{\partial (2\mu S_{13} - \overline{\rho u'w'})}{\partial x} \\ + \frac{\partial (2\mu S_{23} - \overline{\rho v'w'})}{\partial y} + \frac{\partial (2\mu S_{33} - \overline{\rho w'w'})}{\partial z} + \rho g_z \end{aligned} \quad (2.14)$$

The Reynolds Stress tensor is given as follows:

$$\begin{bmatrix} \tau_{11} & \tau_{12} & \tau_{13} \\ \tau_{21} & \tau_{22} & \tau_{23} \\ \tau_{31} & \tau_{32} & \tau_{33} \end{bmatrix} = - \begin{bmatrix} \overline{\rho u'u'} & \overline{\rho u'v'} & \overline{\rho u'w'} \\ \overline{\rho v'u'} & \overline{\rho v'v'} & \overline{\rho v'w'} \\ \overline{\rho w'u'} & \overline{\rho w'v'} & \overline{\rho w'w'} \end{bmatrix} \quad (2.15)$$

The correlation terms, $\overline{u'u'}$, $\overline{v'v'}$, $\overline{w'w'}$, $\overline{u'v'}$, $\overline{u'w'}$, and $\overline{v'w'}$ are to be modeled since the turbulent components cannot be solved fully using the statistical approach. Reynolds Averaging introduced six unknowns in addition to the variables, U , V , W , and P . In all, there are thus ten unknowns but only four equations (Eqs. (2.11) to (2.14)). The function of turbulence modeling is to devise approximations for the unknown correlations in terms of the flow properties that are known, so that a sufficient number of equations results to make solution possible. With such approximations, the system of equations is now closed (Wilcox [24]). The turbulent stresses can be modeled using the Boussinesq approximation as follows:

$$-\overline{\rho u'v'} = \mu_T \left(\frac{\partial U}{\partial y} + \frac{\partial V}{\partial x} \right) \quad (2.16)$$

$$-\rho\overline{u'u'} = -\frac{2}{3}\rho k \quad (2.17)$$

where μ_T is the Eddy Viscosity and k is the turbulence kinetic energy—namely, $k = \frac{1}{2} (\overline{u'u'} + \overline{v'v'} + \overline{w'w'})$. All the other turbulent stress entities can be similarly obtained as in Eqs. (2.16) and (2.17).

An eddy viscosity equation relating μ_T and k adds another equation. If the k - ϵ turbulence model is used, the system can finally be closed with the two additional equations given for the turbulence kinetic energy (k) and the dissipation rate (ϵ). The unknown variables/parameters finally are U , V , W , P , μ_T , k , and ϵ (seven in number). The available equations consist of four Navier-Stokes equations, one eddy viscosity equation, one equation for k , and one for ϵ (a total of seven equations). Hence, the system is closed. Chay et al. [4] discussed the use of a turbulence model specific to an impinging jet flow; there, the RNG (Renormalization Group) k - ϵ model was employed.

The closure coefficients for the RNG k - ϵ model are: $C_\mu = 0.0845$, $\sigma_k = 0.7194$, $\sigma_\epsilon = 0.7194$, $C_{\epsilon 1} = 1.42$, $C_{\epsilon 2} = 1.68$, $\eta_0 = 4.38$, and $\beta = 0.012$, where σ_k is associated with the transport equation for k while all the other model coefficients are associated with the transport equation for ϵ . This fully defines the closed set of governing equations for the thunderstorm downburst problem.

2.3 Computational Framework

2.3.1 Domain and Meshing

The closed set of equations developed are to be solved within a physical domain with appropriately specified boundary conditions. Axisymmetric flow conditions may be assumed for a stationary impinging jet. The problem is, thus, solved in a two-dimensional computational domain. Only one-half of the two-dimensional plane including the axis of symmetry is employed. Figure 2.1 shows a sketch of the computational domain and associated boundary conditions. Details related to the boundary conditions are given in Table 2.1.

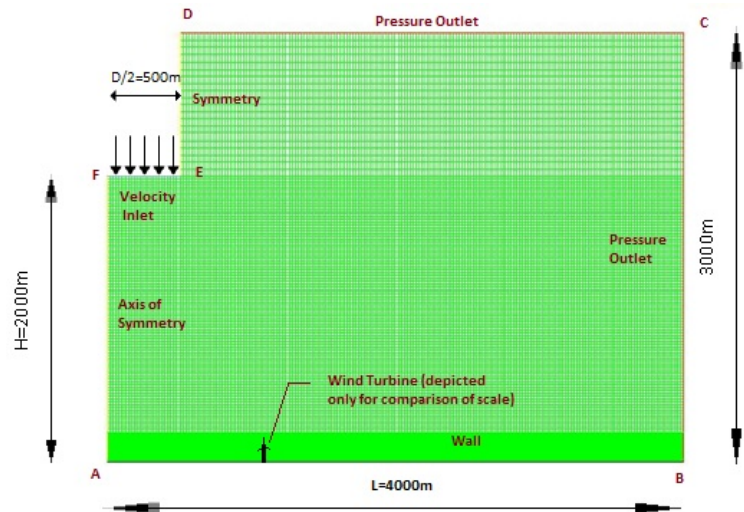


Figure 2.1: A representative sketch of the computational domain.

In the computational domain, the direction from A to B is the radial direction and that along the axis (i.e., from F to A) is the axial direction for the downburst. A discussion on convergence related to the computational

AB	Wall (no slip, stationary)
BC, CD	Pressure Outlet Backflow turbulence intensity = 1% Backflow hydraulic diameter = D
DE	Symmetry
EF	Velocity Inlet (V_{in} specified) Turbulence intensity = 1% Hydraulic diameter = D
FA	Axis of Symmetry

Table 2.1: Boundary conditions for the computational domain.

grid is presented in Section 2.4.4. The grid defined as Mesh II is chosen for all the simulations. Mesh II has a grid spacing of 5 m in the direction perpendicular to the wall and a very fine spacing close to the wall, to ensure that the dimensionless wall distance, y^+ , is below 3. The grid spacing in the radial direction (AB) is 5 m for the entire mesh; hence, except in a region of about 20 m from the wall, the domain has a uniform grid of 5 m \times 5 m over the entire computational domain.

2.3.2 Solution Methodology

2.3.2.1 CFD Theory and Implementation

The mathematical problem at hand, involving solution of the set of partial differential equations, must be addressed computationally by discretizing the independent variables representing space and time. By ensuring a relatively fine level of discretization, errors relative to the exact solution can be significantly limited and the numerical solution can be used for practical

purposes such as in wind turbine loads studies. The computational domain is discretized using the mesh described earlier and the equations are integrated over each of the cells; solution is achieved using the Finite Volume Method. The derivative terms and others in the governing differential equations are represented using Taylor series expansions; then, solution of the resulting series of algebraic equations yields the numerical solution of all the physical variables (such as fluid velocities) in space and as time series.

2.3.2.2 Implementation in FLUENT

Table 2.2 provides some details on the models, schemes, and other information used with the commercial software, FLUENT 12.0, to carry out all the simulations.

2.3.3 Simulations

Both time-dependent and steady-state simulations are carried out. The time-dependent simulations are more appropriate to describe the downburst event; hence, these simulations were used for the model development. This is discussed further in subsequent sections.

2.4 Model Development

2.4.1 Developing an application specific model

Any model intended to describe a physical (fluid dynamics) phenomenon needs to represent salient characteristics of the physics of the phenomenon.

General	Pressure-based solver 2D Axisymmetric Space Gravitational acceleration = 9.81 m/s ²
Models	Viscous <i>k</i> - ϵ (2-equation) RNG model Enhanced wall treatment Default model constants
Materials	Air Density = 1.225 kg/m ³ Dynamic Viscosity = 1.7894e-05 kg/m-s
Solution Methods	Pressure-Velocity Coupling: SIMPLE Scheme Spatial Discretization: Gradient - Least Squares Cell-Based Pressure - Standard Momentum - QUICK Turbulence Kinetic Energy - QUICK Turbulence Dissipation Rate - QUICK Transient Formulation: Second-Order Implicit
Solution Controls	Default Under-Relaxation Factors
Monitors	Residual Convergence Criteria at 1e-5
Run Calculation	Time Step Size = 0.5 sec Max Iterations/Time Step = 80

Table 2.2: FLUENT Simulation parameters.

Thunderstorm downbursts can cause highly complex flow fields. As discussed, past research studies have simulated downburst-like flows using various methods—for example, based on impinging jets, buoyancy-driven flows, etc. Several characteristics of a downburst such as its intensity, translational speed, shape of the velocity profiles, etc. are important to represent realistically in any simulation. Steady-state simulation of an impinging jet on a wall (as described by Chay et al. [4] and by Qu and Wang [18]) has been shown to yield vertical velocity profiles that match observed data quite well. If one were interested in a more

realistic representation of the actual physics of the flow, a buoyancy-driven flow simulation using LES (Anabor et al. [2]) is preferred. In the context of wind turbine loads analysis, realistic representation of the inflow wind velocity field on the turbine rotor is of critical importance. The objective of this study is to develop a CFD model that can provide realistic simulation of the time-varying wind field on a turbine rotor that preserves salient downburst features.

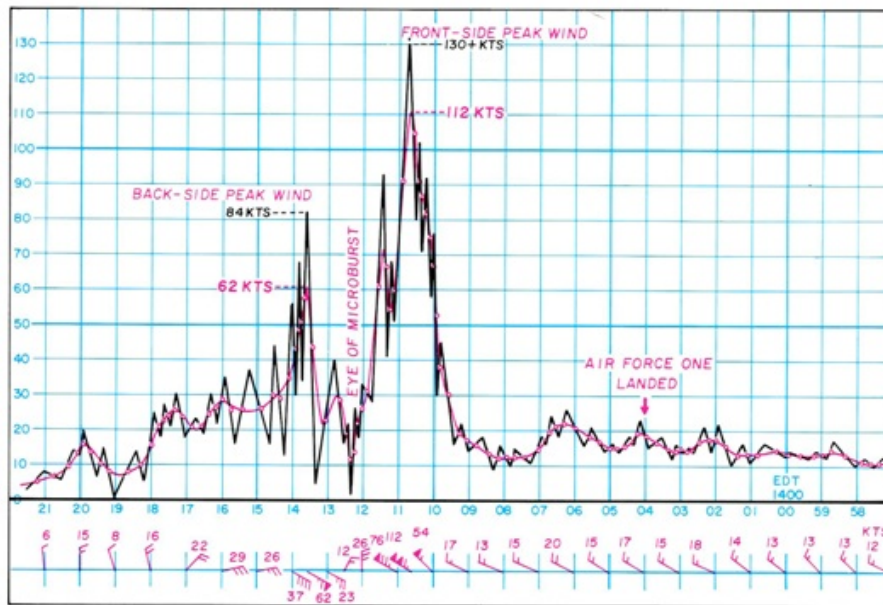


Figure 2.2: Wind speed record during the Andrews AFB microburst recorded on August 1, 1983 (from Fujita [5]).

The Andrews AFB downburst (Fig. 2.2) is one of the best recorded downbursts in the literature. It shows two noticeable peaks in the wind speed record during the downburst. A second smaller peak follows the first larger

one (when read from right to left in the figure). The low wind speed between the peaks corresponds to the eye of the downburst and is similar in effect to the stagnation region at the center of an impinging jet (see Fig. 2.3). The formation of a ring vortex is commonly observed in downbursts (see, for example, Fig. 2.4); the wind speed below the ring is usually the maximum wind speed experienced in the thunderstorm downburst (Fujita [5]). In Fig. 2.4, the downburst axis (not seen in figure) is to the right side of the ring. The ring forms because of the Kelvin-Helmholtz instability that results at the interface of the downburst wind and the ambient wind (Kim and Hangan [11]). The velocity gradient across the interface leads to the ring formation. The difference in magnitude between the two peaks in Fig. 2.2 is due to the effect of both the downburst's translational motion and the ambient wind on the front and rear ring vortices.

Several CFD simulations using FLUENT were carried out by modeling a stationary impinging jet, an impinging jet at steady state, a moving impinging jet, etc. None of these showed reasonable similarity with the Andrews AFB data. Although observations similar to that of Kim and Hangan [11] were noted, such as in the development of quasi-periodic ring vortices at the interface of the ambient wind and the downburst, wind speed time histories did not resemble that recorded in the Andrews AFB event. This is not surprising for several reasons. First, an impinging jet is only an approximation to the physics associated with downburst flow fields. Second, it is unreasonable to expect to match the complex downburst flow phenomenon, kinetics, and

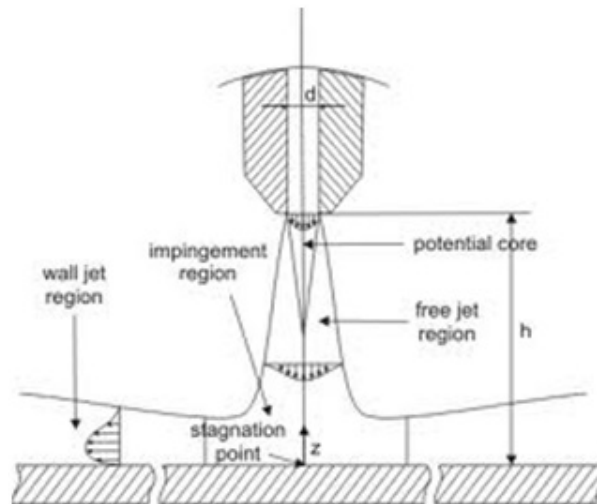


Figure 2.3: Schematic model of an impinging jet showing different regions in the flow field.

movement with a simple stationary jet simulation. Third, any single point's recorded or simulated wind time series is an observer-dependent entity; it is entirely possible that the Andrews AFB downburst record did not capture the ring vortices and it could as well be the case that there were not multiple rings generated during the Andrews AFB downburst. There is not a wealth of good-quality downburst data that can be used to validate computational simulations. Given only the Andrews AFB downburst, other attempts were made to simulate wind speed time series that resembled that record alone.

Assuming that the Andrews AFB downburst record is representative of likely downburst wind speed time histories, a "Paused Downburst" Model is developed to match this record. The idea behind developing a Paused Down-



Figure 2.4: Ring formation at the gust front of a downburst (from Fujita [5]).

burst Model comes from the need to match the Andrews AFB data. Note that the peaks of the AFB data indicate that if a downburst were to pass a wind turbine or observer, one would see a step increase in the wind speed (due to the first peak), then a sudden drop (due to the eye of the downburst), then another step increase but of lower magnitude than the first (due to the second peak) and then a decrease back to the ambient wind. Such steep in-

creases and decreases in the experienced wind speed at a point is possible only if the storm has a profile such as is shown in Fig. 2.5, where the radial velocity is minimum at its center, increases up to a certain radial distance (where it reaches a maximum) and then drops down beyond that distance. Such a radial profile of velocity on both sides of the axis of a downburst will cause two peaks similar to that of the Andrews AFB data which also includes the influence of the ambient wind.

The analytical model developed by Vicroy [23] has a similar radial profile and can as well be used to simulate an Andrews AFB-type wind speed time history. Such a wind field can be produced by CFD simulation of a jet impinging on a flat plate. This impinging jet on a flat plate can be studied either as a time-dependent simulation or at steady state. Both of these types of simulations were carried out and their velocity profiles compared as shown in Figs. 2.6 and 2.7. The radial profiles of the radial velocity for the steady-state simulation are not in good agreement with the actual downburst data or with the analytical model. The radial profiles of the time-dependent simulations, at different time instants before the formation of the secondary ring vortex near the ground, suggest good agreement with the actual downburst data as well as with the analytical model. Hence, a snapshot (Fig. 2.7(a)) of the time-dependent simulation, before the secondary vortex formation, can serve as an alternative (computational) model to the analytical model. Since a snapshot from the simulation represents the model, this is termed a “Paused Downburst” model. In a general sense, it may be stated that this snapshot of the time-

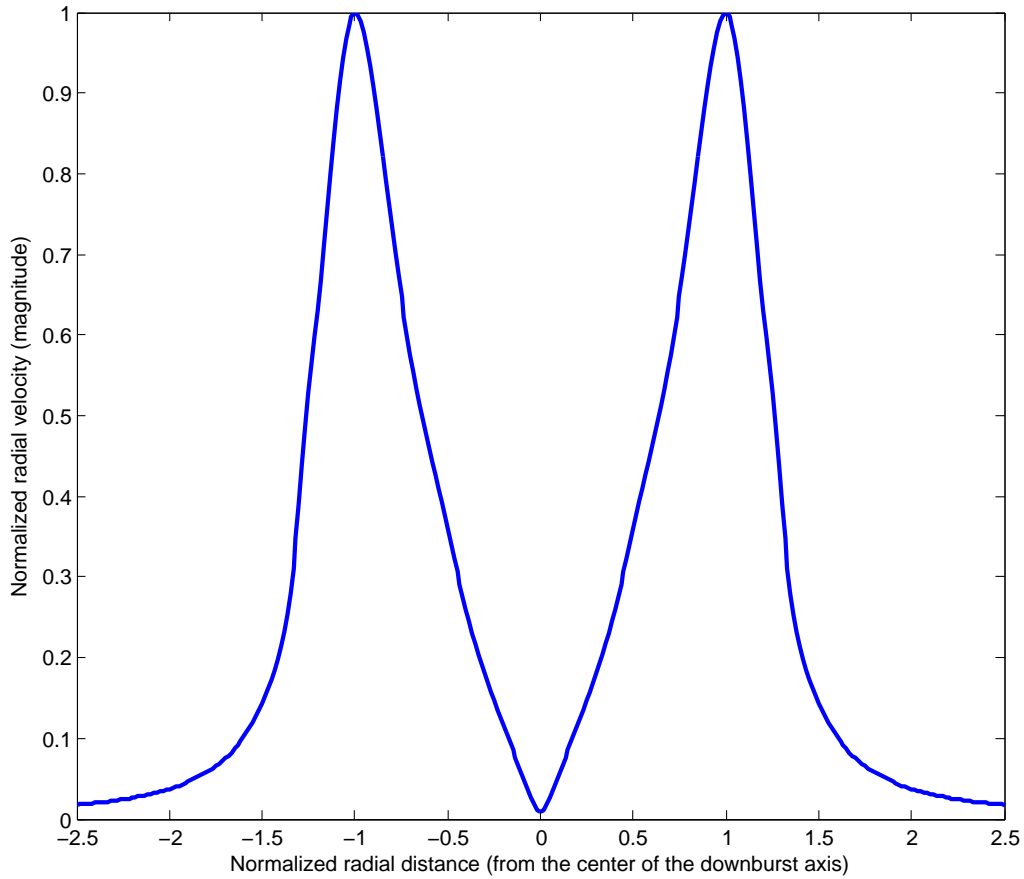
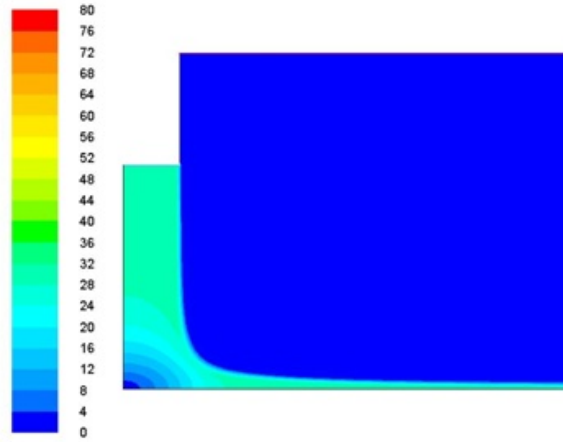
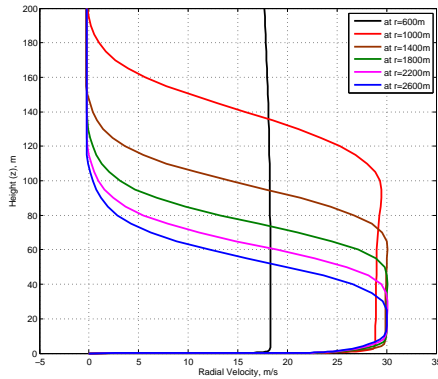


Figure 2.5: Normalized radial velocity profiles for a Paused Downburst Model.

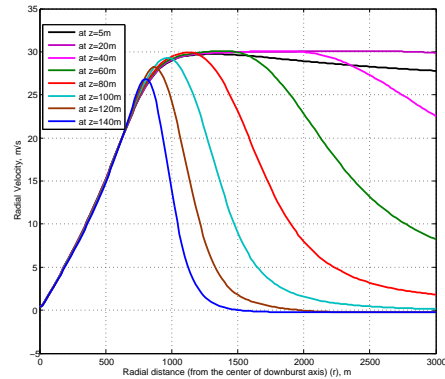
dependent simulation captures the overall behavior of the downburst in an average sense. Figure 2.23 (discussed later) shows that the Paused Downburst model offers a close match with the Andrews AFB downburst wind speed time history (note that the Andrews AFB downburst data points in that figure were extracted from the original figure (Fig. 2.2)).



(a) Contours of velocity magnitude (m/s) at steady state.



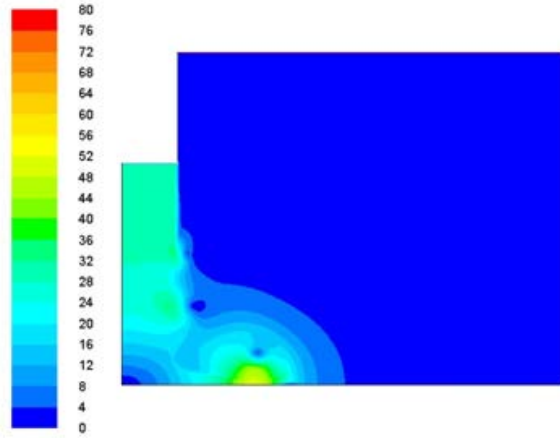
(b) Radial velocity profile variation with height from a steady-state simulation.



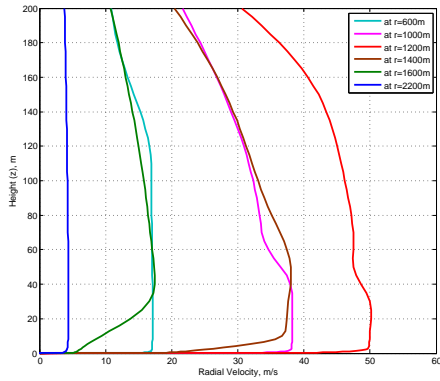
(c) Radial velocity profile variation with radial distance for a steady state simulation.

Figure 2.6: Velocity fields resulting from a steady-state simulation.

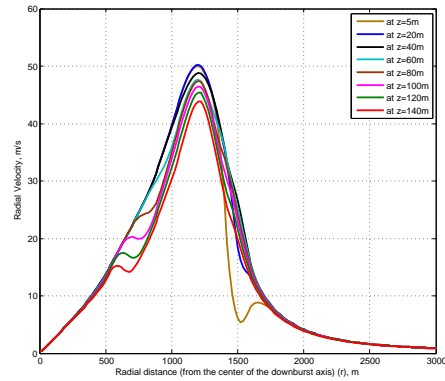
Note that the Paused Downburst model is similar to the analytical model; it is merely an alternative approach for generating a downburst wind velocity field. Note too that the Paused Downburst model does not take into



(a) Contours of velocity magnitude (m/s) for a paused snapshot of a simulation.



(b) Radial velocity profile variation with height for a paused snapshot.



(c) Radial velocity profile variation with radial distance for a paused snapshot.

Figure 2.7: Velocity fields resulting from a paused snapshot of a simulation.

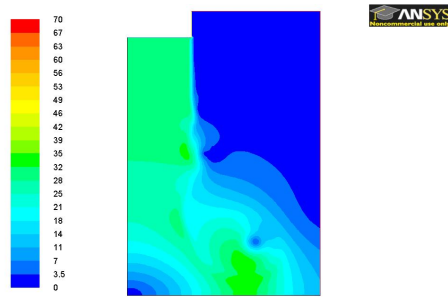
account possible translation of the downburst; any translational effects of the downburst need to be superimposed onto the model separately.

2.4.2 Description of the “non-turbulent” wind field

The Reynolds number of the flows in a downburst are on the order of millions. Such flows can be reasonably accurately modeled only using LES; DNS is not a feasible option and statistical modeling would involve gross approximations. Nevertheless, statistical modeling may be used to compute time-averaged components of flow field variables (as was described in Eqs. (2.7) to (2.10)). The turbulent or fluctuating components of the wind velocities are computed using standard turbulence power spectral densities and coherent functions. This is discussed in Chapter 3.

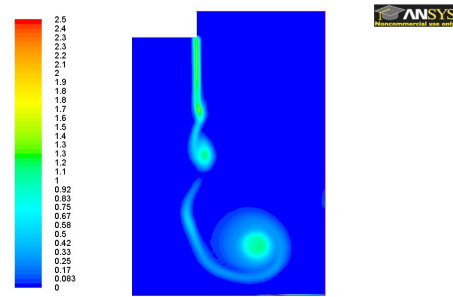
2.4.3 Solution convergence and choice of inlet velocity profile

Since the downburst flow has a very high Reynolds number, the computational domain requires a very fine grid size and a small time step for accuracy. In addition, formation of the ring vortex (as seen in Fig. 2.7(a)) at the interface of the downburst vertical jet and the ambient air, further complicates the flow field. A resolution of the finer details of this ring in this high Reynolds number flow is impractical due to computational and other constraints. As the grid size and time step are made smaller, the ring (vorticity) is better resolved but these show up small-scale effects that influence the final solution in a cumulative sense. This can be seen in Fig. 2.8 where three different meshes with 10 m, 5 m, and 2 m uniform grid spacing were employed to study the influence of grid size on solution convergence. The problem identified can be overcome if a weaker ring is generated.



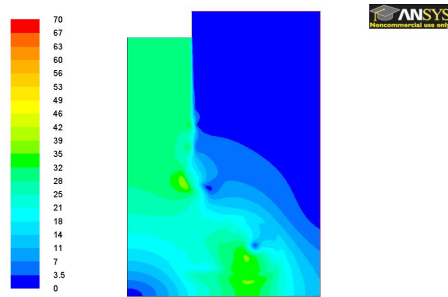
Contours of Velocity Magnitude (m/s) (Time=7.5000e+01)
ANSYS FLUENT 12.1 (axi, dp, pbns, mgke, transient) Aug 20, 2011

(a) Velocity contours for a uniform grid size of 10 m.



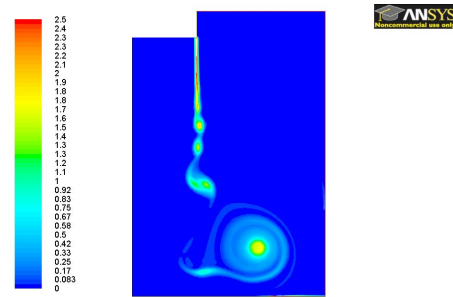
Contours of Vorticity Magnitude (1/s) (Time=7.5000e+01)
ANSYS FLUENT 12.1 (axi, dp, pbns, mgke, transient) Aug 20, 2011

(b) Vorticity contours for a uniform grid size of 10 m.



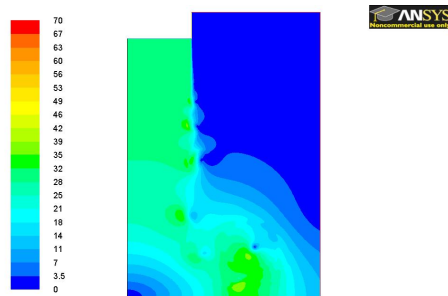
Contours of Velocity Magnitude (m/s) (Time=7.5000e+01)
ANSYS FLUENT 12.1 (axi, dp, pbns, mgke, transient) Aug 20, 2011

(c) Velocity contours for a uniform grid size of 5 m.



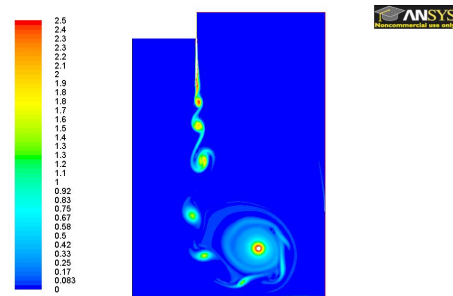
Contours of Vorticity Magnitude (1/s) (Time=7.5000e+01)
ANSYS FLUENT 12.1 (axi, dp, pbns, mgke, transient) Aug 20, 2011

(d) Vorticity contours for a uniform grid size of 5 m.



Contours of Velocity Magnitude (m/s) (Time=7.5000e+01)
ANSYS FLUENT 12.1 (axi, dp, pbns, mgke, transient) Aug 20, 2011

(e) Velocity contours for a uniform grid size of 2 m.



Contours of Vorticity Magnitude (1/s) (Time=7.5000e+01)
ANSYS FLUENT 12.1 (axi, dp, pbns, mgke, transient) Aug 20, 2011

(f) Vorticity contours for a uniform grid size of 2 m.

Figure 2.8: Grid dependency of solution with a uniform inlet velocity

The strength of the ring vortex that forms at the interface of the jet and the ambient air is a direct function of the difference in magnitude of the velocity (i.e., the vorticity) at the interface. If the inlet velocity has a profile with a higher magnitude at the interface, a stronger ring results. The shape of the profile of the inlet velocity influences the strength of the ring formed; this, in turn, controls the convergence of the solution with respect to grid and time step. It can be assumed that if the magnitude of the velocity at the interface is zero, a very weak ring will result. At the interface, such a velocity profile can have different slopes; i.e., slopes at the intersection with the horizontal axis of the plot in Fig. 2.9. The effect of slope was studied by running simulations using different shapes for the inlet velocity. Changes in slope did not show any significant influence on the solution. Simulation results for a parabolic inlet velocity profile are presented in Fig. 2.10. It can be confirmed that the solution converges with respect to grid size. A parabolic inlet velocity profile was chosen for all other simulations used for development of the Paused Downburst Model.

2.4.4 Choice of grid and time step

Generally, as in traditional approaches to CFD as well as with any computational numerical problems, a converged solution is expected to result as the grid size and/or time step are reduced systematically. A series of simulations involving different meshes with different grid sizes and different time steps were carried out. The computational domain chosen for these simulations

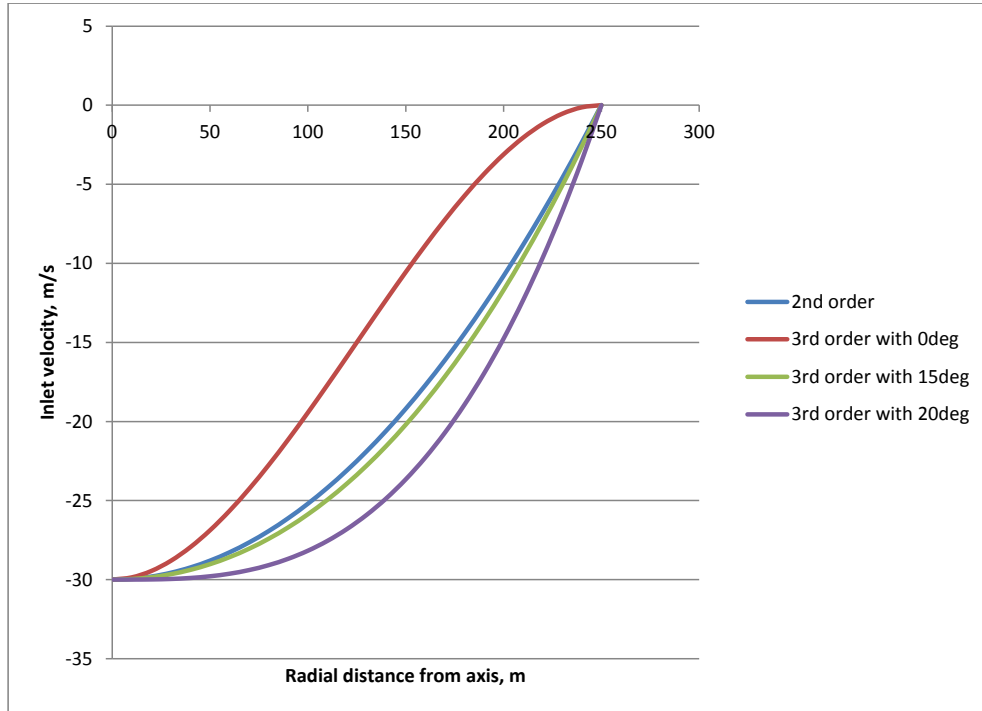
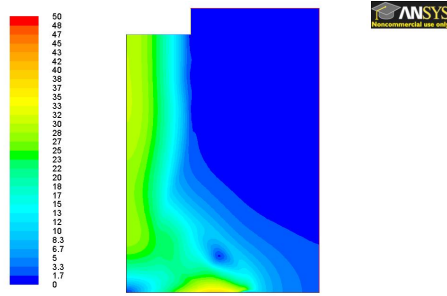


Figure 2.9: Inlet velocity profiles with zero velocity at interface

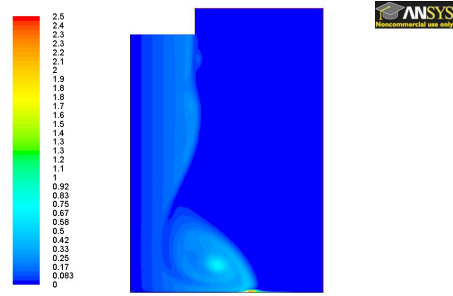
was similar to that those used in Fig. 2.10

Three meshes, Mesh I, Mesh II, and Mesh III, each with uniform grid sizes of 10 m, 5 m, and 2 m, respectively, were created. The radial velocity plot shown in Fig. 2.11 suggests that a grid size of 5 m would be acceptable since the solution with the 2 m and 5 m grids is almost the same. The mesh with the 5 m grid spacing was chosen for simulations with different time steps, $\Delta t = 0.1$ s, 0.25 s, 0.5s, 1.0 s, and 2.5 s. The radial velocity plot (Fig. 2.12)



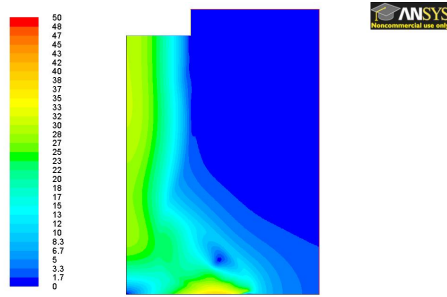
Contours of Velocity Magnitude (m/s) (Time=8.5000e+01)
ANSYS FLUENT 12.1 (axi, dp, pbns, mgke, transient) Aug 23, 2011

(a) Velocity contours for a uniform grid size of 10 m.



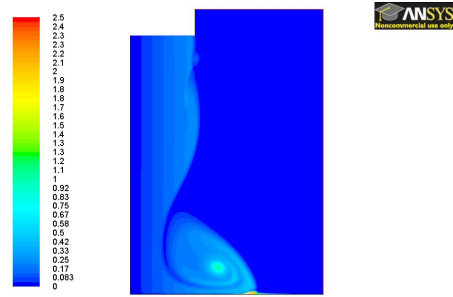
Contours of Vorticity Magnitude (1/s) (Time=8.5000e+01)
ANSYS FLUENT 12.1 (axi, dp, pbns, mgke, transient) Aug 23, 2011

(b) Vorticity contours for a uniform grid size of 10 m.



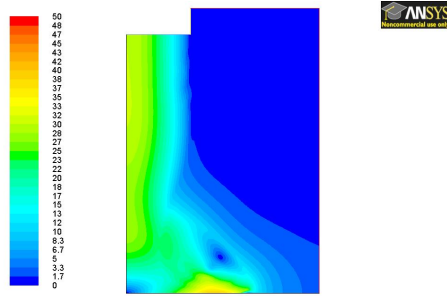
Contours of Velocity Magnitude (m/s) (Time=8.5000e+01)
ANSYS FLUENT 12.1 (axi, dp, pbns, mgke, transient) Aug 22, 2011

(c) Velocity contours for a uniform grid size of 5 m.



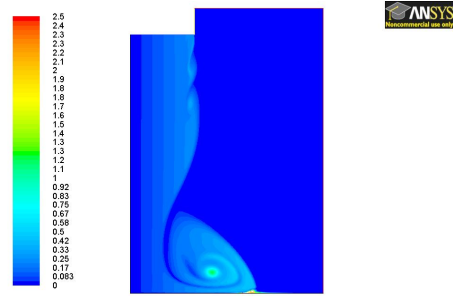
Contours of Vorticity Magnitude (1/s) (Time=8.5000e+01)
ANSYS FLUENT 12.1 (axi, dp, pbns, mgke, transient) Aug 22, 2011

(d) Vorticity contours for a uniform grid size of 5 m.



Contours of Velocity Magnitude (m/s) (Time=8.5000e+01)
ANSYS FLUENT 12.1 (axi, dp, pbns, mgke, transient) Aug 22, 2011

(e) Velocity contours for a uniform grid size of 2 m.



Contours of Vorticity Magnitude (1/s) (Time=8.5000e+01)
ANSYS FLUENT 12.1 (axi, dp, pbns, mgke, transient) Aug 22, 2011

(f) Vorticity contours for a uniform grid size of 2 m.

Figure 2.10: Grid dependency of solution with a parabolic inlet velocity profile

suggests that the time step of 0.5 s would make a good choice.

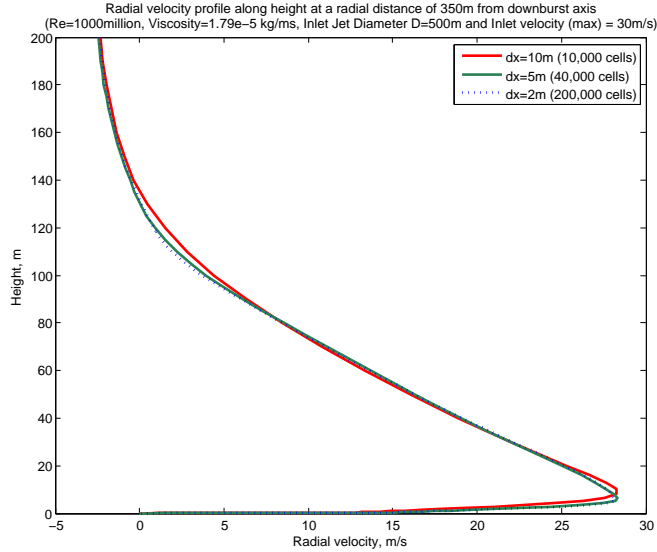


Figure 2.11: Tests for the choice of grid.

2.5 The Paused Downburst Model

2.5.1 Time-independent model

The time-independent Paused Downburst model is simply the spatial distribution of velocities (at discrete locations) at a given time instant in an unsteady simulation of jet impingement as was discussed earlier. The idea has been taken from the observation that the velocity profiles of the flow field a few instants before the formation of the secondary vortex (near the wall) show good agreement with actual downburst data recorded in the past (Hjelmfelt [7]). The computational domain shown in Fig. 2.13 is used for all

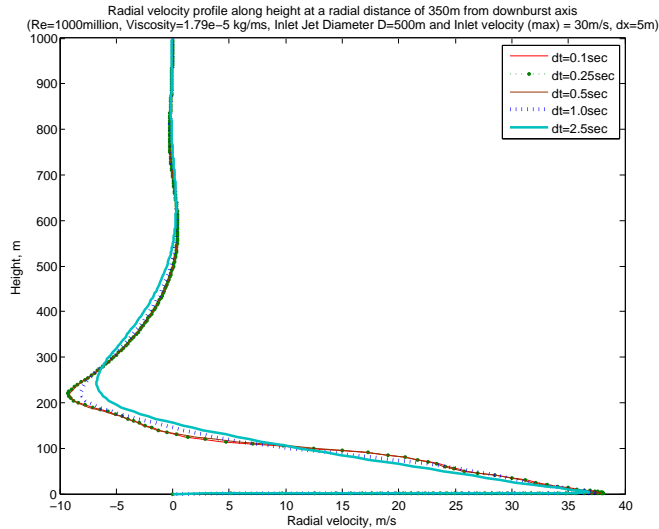


Figure 2.12: TTests for the choice of time step.

the simulations to develop the generalized model (discussed in Section 2.6). In the figure, D represents the diameter of the inlet jet while H represents the height of the origin of the inlet flow from the wall. The axial direction is defined as that parallel to the axis and perpendicular to the wall; the radial direction is defined as that parallel to the wall.

Consider a domain with inlet diameter, $D = 1000$ m, $H = 2000$ m, and with a parabolic inlet velocity profile with maximum velocity, $V_{in,max} = 40$ m/s. The values chosen for these parameters represent real observations discussed by Hjelmfelt [7]. These three entities— D , H , and $V_{in,max}$ —are the input parameters for the CFD simulations carried out using ANSYS FLUENT. The Paused Downburst model results depend on the time at which the simulation is paused. Figure 2.14 shows the snapshot of a simulation paused at 107 s

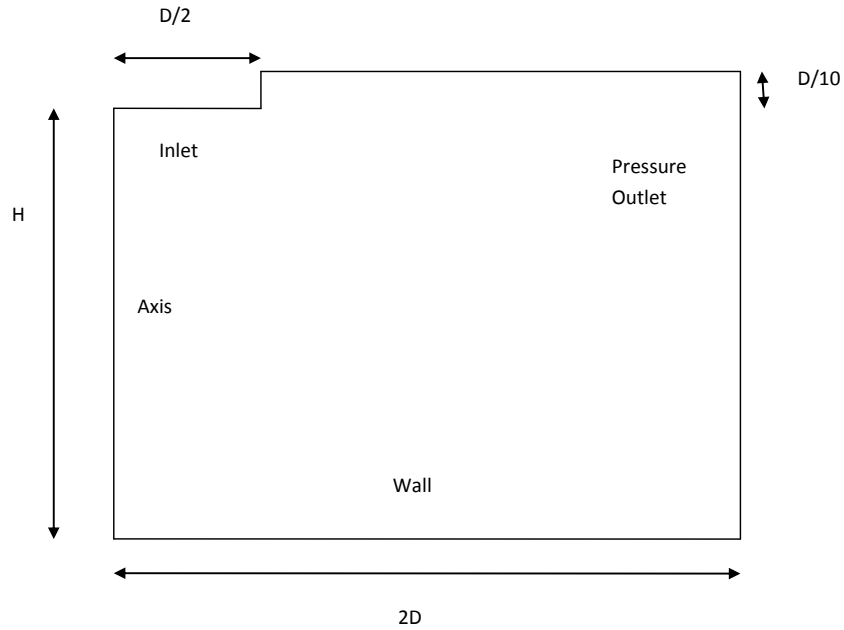
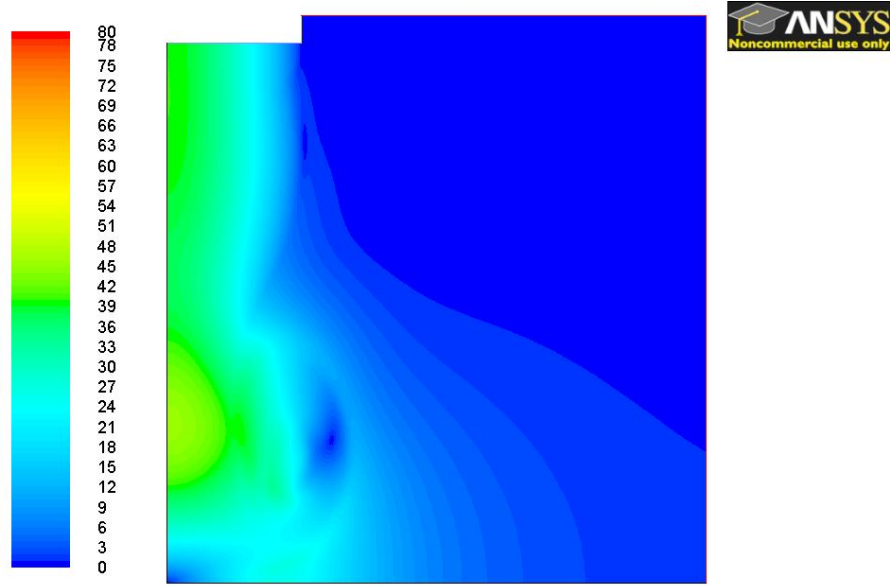


Figure 2.13: Computational domain used for the simulations.

with the above parameters. This snapshot is equivalent to a computational time-independent model of a downburst. This can also be understood as an outcome of the Paused Downburst model for a given set of input parameters.

As stated earlier, the model represents the set of velocity component data in space. The velocity at any point in space has two components—radial and axial. Figures 2.15(a), 2.15(b), 2.16(a) and 2.16(b) show the variations of the velocity components in both directions. In the figures, Z refers to the height in meters from the wall, Z_{Max} is the height at which the overall maxi-

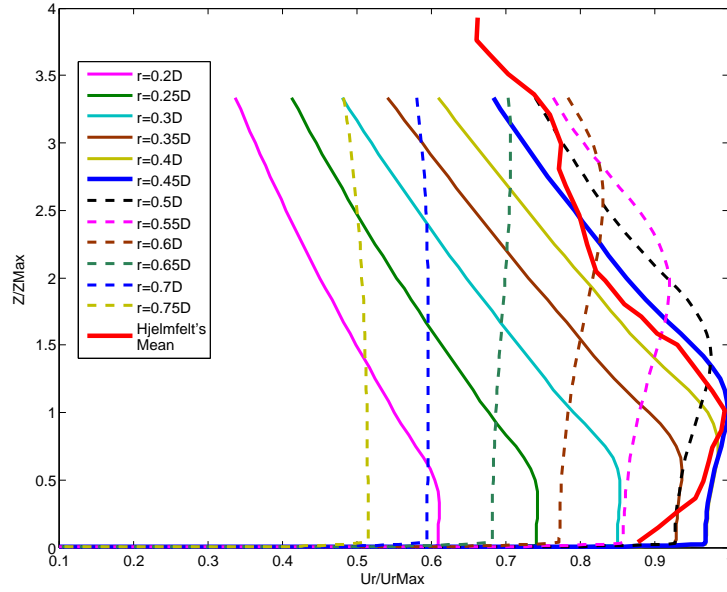


Contours of Velocity Magnitude (m/s) (Time=1.0700e+02) Sep 02, 2011
 ANSYS FLUENT 12.1 (axi, dp, pbns, mgke, transient)

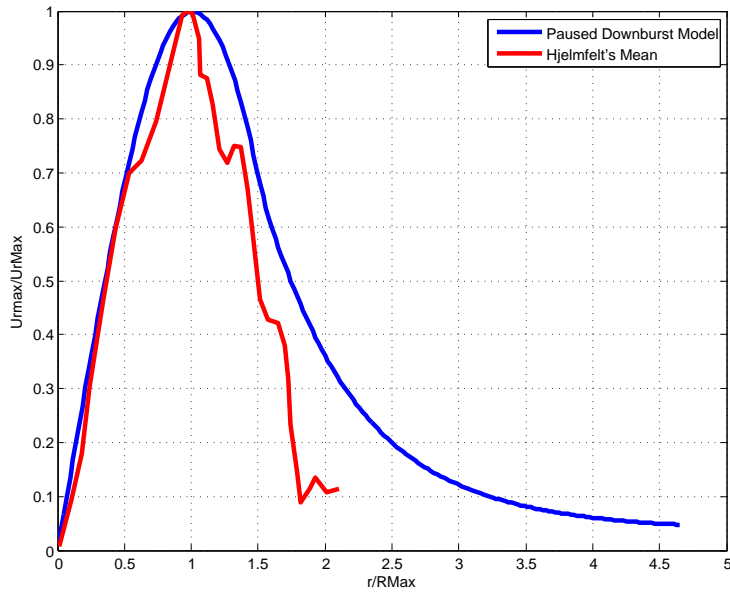
Figure 2.14: Snapshot of a simulation at a paused instant.

mum radial velocity occurs, U_r is the radial velocity, Ur_{max} is the peak radial velocity or the maximum radial velocity at each radial position, $UrMax$ is the overall maximum radial velocity, r is the radial distance in meters from the axis, $RMax$ is the radial position where the overall maximum radial velocity occurs, and U_a is the axial velocity. It is interesting to note in Fig. 2.16(b), where the axial velocity distribution at various heights is presented, that all the profiles change sign at some radial position. This is the position where the downward flow, upon reaching the ground (wall), deflects radially which causes a small axial velocity component in the upward direction. The radial

velocity starts from zero at the axis, reaches a peak and then decreases (at a higher rate than the radial wall jet at steady state). In this example, $UrMax$ occurs at a radial distance of approximately 450 m or $0.45D$ from the axis and $ZMax$ is at about 60 m or $0.06D$ from the wall.

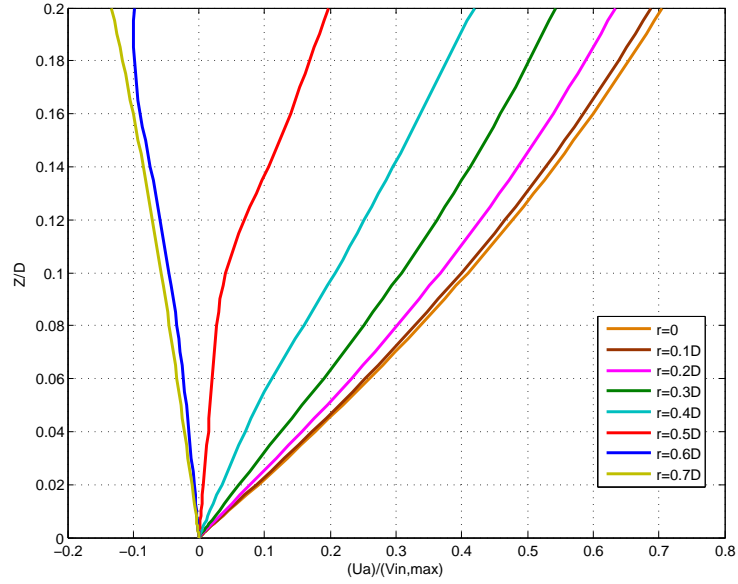


(a) Normalized radial velocity profiles variation with height.

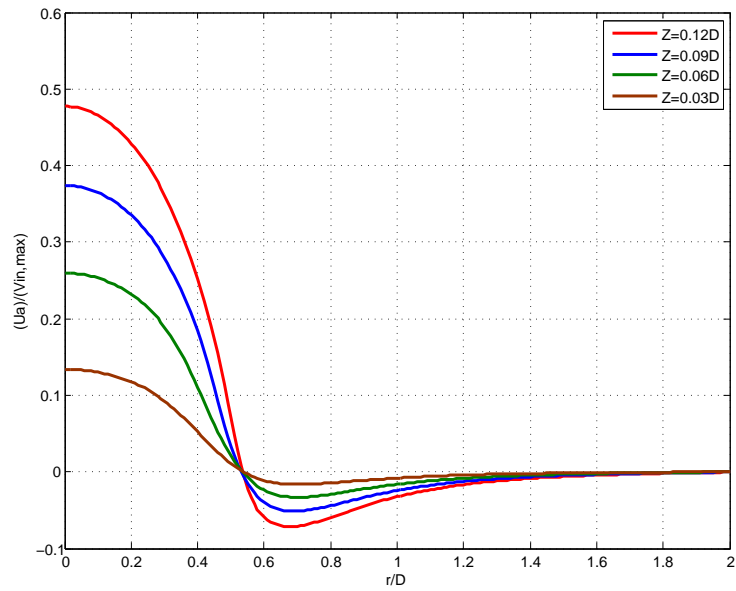


(b) Normalized peak radial velocity profiles variation with radial distance.

Figure 2.15: Radial velocity distributions at the paused time instant (107 s).



(a) Normalized axial velocity profiles variation with height.



(b) Normalized axial velocity profiles variation with radial distance.

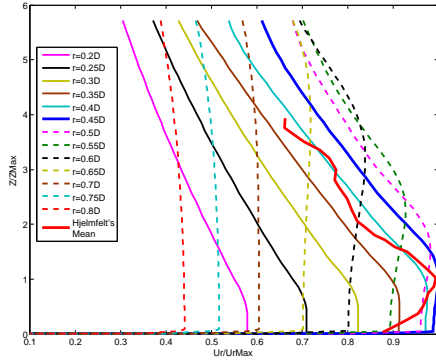
Figure 2.16: Axial velocity distribution at the paused time instant (107 s).

If the paused time instant were chosen as something other than 107 s (see Figs. 2.17 and 2.5.1), then the velocity profiles in space would be slightly different. The input parameters could be changed to yield a different set of velocity profiles. The dependence of the model on these input parameters and the time of pause is used to develop a generalized model later.

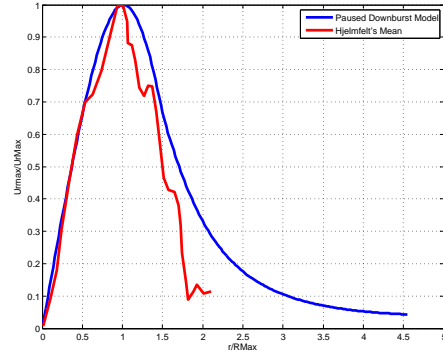
2.5.2 Time-dependent model

The time-independent model discussed in Section 2.5.1 is a static representation of a stationary downburst. In reality, a ring vortex forms in a downburst and moves radially outward from its axis. Also, the intensity of the downburst flow changes with the time. This latter aspect can be taken care of by scaling the model output velocity field data from the simulation using a time-dependent amplitude modulation function. Consideration of the radial evolution of the downburst, however, requires the development of a spatial velocity field at each time step created by moving $RMax$ away from the axis; this requires significantly greater computational effort. It can also not be achieved by an unsteady CFD simulation because the velocity profiles after the formation of a secondary ring vortex near the ground do not match actual downburst data.

The evolution of $RMax$ with time and development of the velocity field at every time step can be achieved by using normalized profiles from the time-independent Paused Downburst model. What is needed is that the normalized shape of the velocity profiles at any time step must be similar

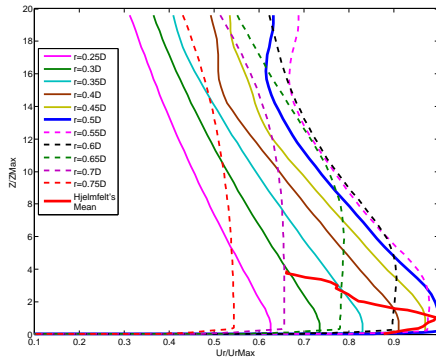


(a) Normalized radial velocity profiles variation with height.

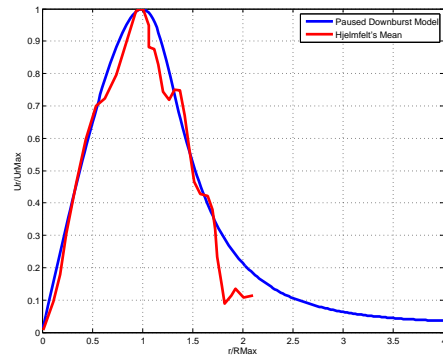


(b) Normalized peak radial velocity profiles variation with radial distance.

Figure 2.17: Velocity distributions at the paused time instant (109 s)



(a) Normalized radial velocity profiles variation with height.



(b) Normalized peak radial velocity profiles variation with radial distance.

Figure 2.18: Velocity distributions at the paused time instant (113 s)

to that of the time-independent model. As time elapses, the flow that is impinging on the ground rushes radially outward. Hence, with time, $RMax$ and hence the spatial extent of the storm's influence will increase. In all the simulations, the velocity data have been collected at a 10 m spacing in the radial direction. Hence, when $RMax$ increases, the number of grid points at which velocity values need to be defined also increases. For example, if $RMax = 450$ m, about 90 data points representing 900 m of radial extent are sufficient, but when $RMax = 800$ m, about 160 data points are required. Developing velocity profiles at each time step requires interpolation of the normalized velocity profiles at intermediate radial positions. This is discussed next.

Consider a peak radial velocity distribution at any time instant. This distribution gives information about the peak radial velocity at each radial position from the axis of the downburst. Each peak radial velocity in the distribution is associated with a separate vertical profile of the radial velocity. Hence, in order to develop a spatial velocity distribution at any specified time instant, one needs to define the vertical velocity distribution (profile) that must be used for all the peak radial velocities representing various radial positions in the non-normalized peak radial velocity distribution plot. The peak radial velocities corresponding to any (non-dimensional) radial position can be read off from the approximate analytical profiles (see Fig. 2.19) developed for the peak radial velocity distribution. The left half of this analytical profile (Fig. 2.19(a)) can be well approximated by a polynomial (Equation (2.19)) fit

while the right half (Fig. 2.19(b)) is described by an exponential decay function as follows:

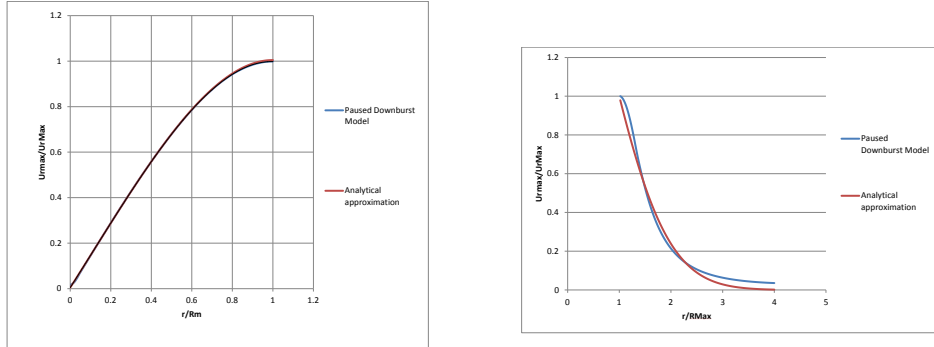
$$u(r) = e^{\left\{\frac{1-r^{1.75}}{1.65}\right\}} \quad (2.18)$$

The polynomial can be expressed as:

$$u(r) = -0.607r^3 + 0.199r^2 + 1.401r + 0.005 \quad (2.19)$$

In Fig. 2.19(b), the variation takes the form shown in Eq. (2.18). Note that vertical profiles for the peak radial velocity are available only for a few peak radial velocity values, which are obtained from the time-independent model. Hence, the vertical profiles for peak radial velocity values other than those available are obtained by linear interpolation using the available profiles; the same applies to the axial velocity profiles as well.

Figures 2.20, 2.21, and 2.22 illustrate an example of the development of a time-dependent Paused Downburst model. The paused time instant is at 107 s as discussed earlier. The axial velocity distributions are not shown as they do not have any features that are especially significant in terms of variation with time. In the case of the radial velocity profiles, however, it must be ensured that the normalized peak radial velocity distribution has the same shape for all times, to ensure model validation with actual downburst data. The axial velocity profiles variation with height at different radial positions are also obtained through interpolation. In the current example, a linear variation



(a) Analytical approximation for the left half.

(b) Analytical approximation for the right half.

Figure 2.19: Normalized peak radial velocity distributions.

of $RMax$ with time is chosen, as described in Fig. 2.20. It is evident that the normalized profiles (Fig 2.21(a)) are the same at all times but the non-normalized profiles (Fig 2.21(b)) are expectedly different since $RMax$ increases with time. Figure 2.22 shows vertical profiles of the peak radial velocity at three different times. It is noted that more grid points (data points) are to be evaluated as time elapses. This is because the storm is expanding radially and because of the needed interpolation of profiles at the desired radial positions.

Notice that at time, $t = 0$ (see Fig. 2.22(a)), the magnitude of the radial velocity is non-zero; this does not make sense physically. Although the model described thus far has most of the aspects of the unsteady downburst phenomenon, two additional characteristics that account for time dependence of the intensity of the storm and the storm's translational velocity have not been incorporated. In the wind turbine load simulations, time dependence of

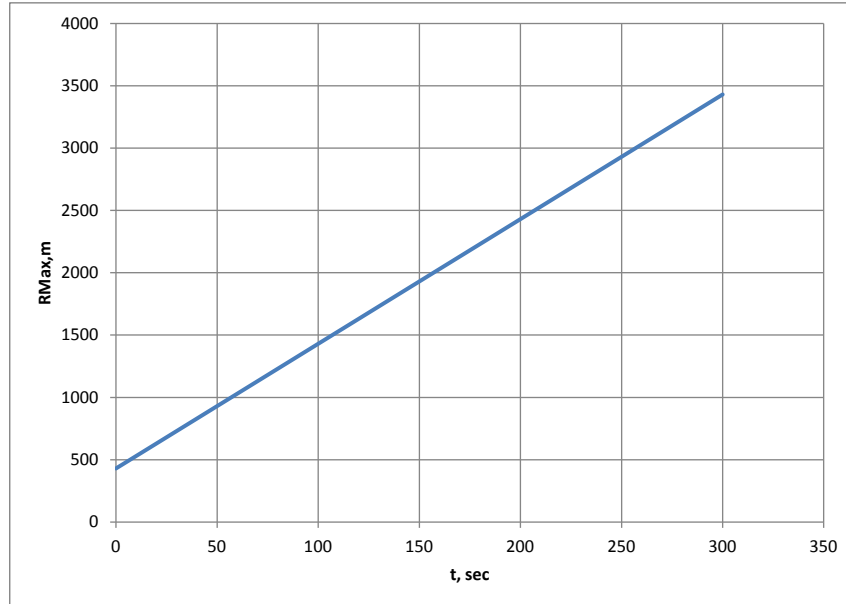
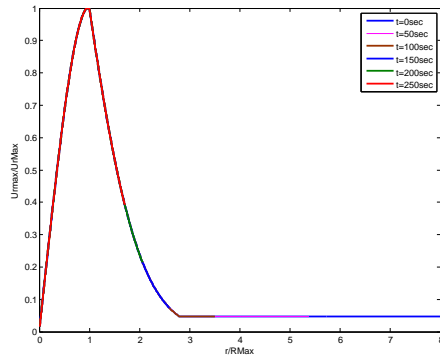
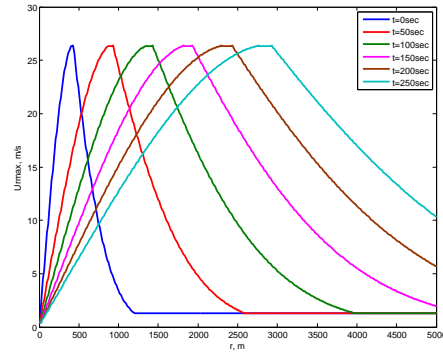


Figure 2.20: Variation of $RMax$ with time.

the intensity of the downburst will be taken care of by modulating the wind field spatial data with a time-varying intensity function—for instance, this intensity function can be modeled by a half-cycle sine pulse with its peak intensity at some specified time (the mid-point of the intensity function). Such an intensity function would take on a zero value at $t = 0$; hence, the velocity field would be zero initially as desired. As time progresses, the intensity would increase, reach a maximum, and then decrease. Hence, by using such intensity functions, representative spatial profiles from the CFD simulation can be converted to a time series of downburst winds that are physically sensible. The translational velocity of the storm will be used in the wind turbine loads



(a) Normalized radial velocity profiles at different time instants.



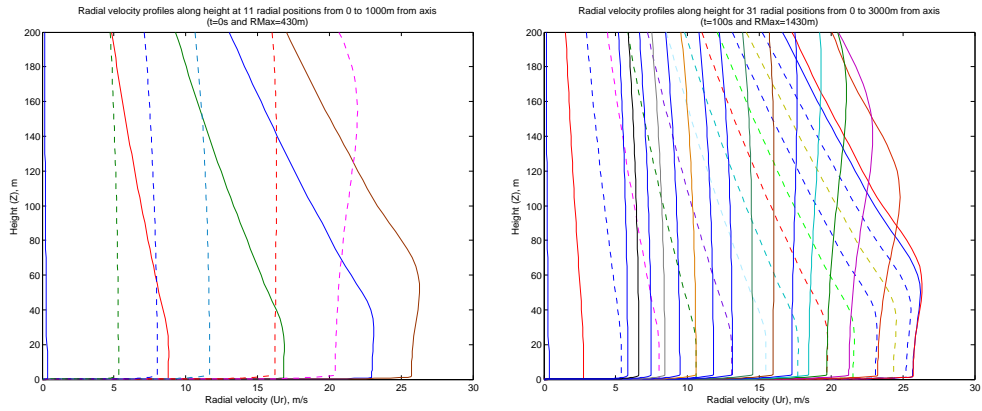
(b) Non-normalized radial velocity profiles at different time instants.

Figure 2.21: Peak radial velocity distributions for the time-dependent model.

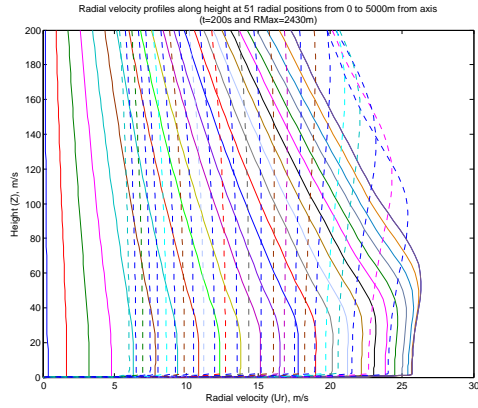
studies to establish the position of the downburst axis at any time instant. This is discussed later.

2.5.3 Validation of the model

Downburst data available in the literature are not sufficient to fully describe time-dependent characteristics of the storm. Hence, the goal was to develop a time-independent model (from CFD simulations) that could be validated against actual data; time-dependent characteristics could be added later as described. This has led to the development of the Paused Downburst model with time-dependent characteristics incorporated into that model as described in Section 2.5.2. Before using the velocity profiles from the Paused Downburst model for any engineering application, it is important to validate the velocity data against any available downburst data. Hjelmfelt [7] presented



(a) Profiles at $t = 0$ s and $RMax = 430$ m. (b) Profiles at $t = 100$ s and $RMax = 1430$ m.



(c) Profiles at $t = 200$ s and $RMax = 2430$ m.

Figure 2.22: RRadial velocity profiles variation with height for the time-dependent Paused Downburst model.

observations and characteristics from several recorded downbursts; a resulting “mean” radial velocity profile showing variation with height and radial distance was also presented. This mean profile is thought to be representative of all the recorded downbursts of the study.

Figures 2.15, 2.17, and 2.5.1 that show the Paused Downburst model’s radial velocity distributions also include Hjelmfelt’s mean profiles. It is noted that the flow field based on the model paused at 107 s matches the mean from observations better than that at other time instants. Hence, it is noted that the adequacy of validation of the Paused Downburst model against data depends on the time of the downburst pause. It is important to note that Hjelmfelt’s mean profiles represent only a few downbursts and are applicable to a specific location and period. Hence, other pause times of the model developed here, although not in good agreement with the Hjelmfelt’s data, might still be realistic models for use in downburst simulations. We note that a pause time beyond the formation of the secondary ring vortex near the wall is not a good choice because a secondary ring significantly distorts the radial distribution and, hence, cannot be validated.

An important feature of the Paused Downburst model’s output the output time series that can be at a specified location. The ability to generate such time series led to the development of the model in the manner described rather than from a steady-state simulation of a wall jet. Figure 2.23 shows a comparison of the time series created by the Paused Downburst model at a specified location and the time series recorded during the Andrews AFB

downburst (Fig. 2.2). Here, the leverage in superposing the ambient wind speed on to the downburst wind field was used to match the Andrews AFB data. We see that the model-generated time series matches characteristics of the observed data quite well; such comparisons serve to support use of the Paused Downburst model for engineering applications where wind speed time series are needed as in wind turbine loads analyses.

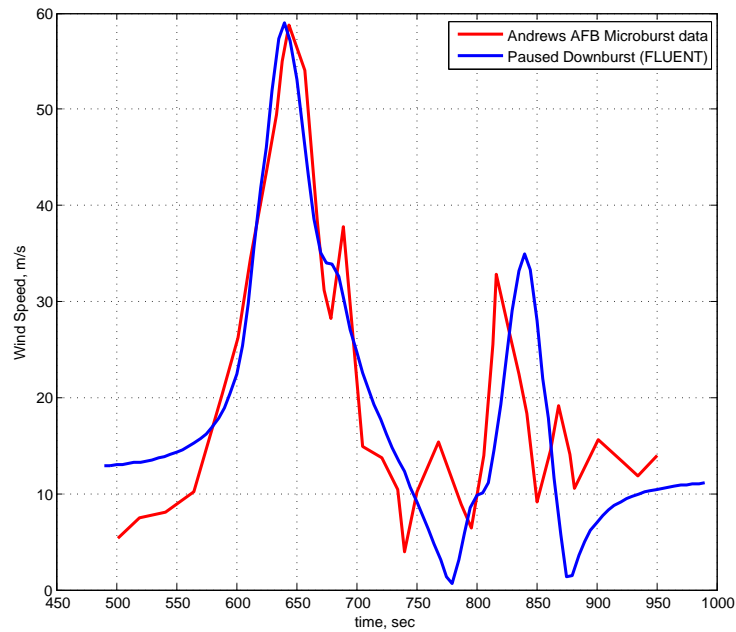


Figure 2.23: Comparison of a wind speed time series resulting from the Paused Downburst model versus the Andrews AFB data.

2.5.4 Limitations of the model

While the Paused Downburst model has been seen to offer comparable wind speed time series characteristics to those in recorded data such as from

the Andrews AFB microburst, it does not necessarily represent the entire time-dependent downburst phenomenon. Moreover, Fig. 2.5.1 suggests that vertical profiles of the radial velocity do not match observed data adequately for all pause times; they are acceptable for our current application in wind turbine loads analysis. Because the Paused Downburst model was developed with the intent of representing the Andrews AFB data, it may not match, as effectively, downbursts that display other characteristics such as the occurrence of multiple ring vortices at or near the ground, the effect of an storm translation, etc. There are not a sufficient number of real downburst records available to establish the effects of these various characteristics on model-generated wind speed time series. Another limitation of the model arises from the basic physics assumptions used to simulate the flow; since the model is based on a momentum flux-driven flow (jet impingement), it does not provide any information related to temperature and precipitation. Finally, an assumption made in the development of this model is that the flow field is axisymmetric; downbursts that do not touch down normal to the ground and those that translate or move do no generate axisymmetric flow fields.

2.6 Generalized procedure to simulate downbursts using the “Paused Downburst” technique

We describe here a general procedure or algorithm to simulate a thunderstorm downburst-like event based on a set of input parameters using the Paused Downburst model. As indicated in Fig. 2.24, the final output param-

eters that define the characteristics of the simulated downburst are $UrMax$, $ZMax$, and $RMax$, which were defined in Section 2.5.1. These model output parameters depend on (i) Vin,max and D/H , which are input parameters for the CFD simulation; and (ii) an intermediate parameter, the time of the downburst pause, tp (sec). The output and intermediate parameters are written in non-dimensional form as follows: $tp^* = \frac{tp \cdot Vin,max}{H}$; $UrMax^* = \frac{UrMax}{Vin,max}$; $ZMax^* = \frac{ZMax}{D}$; and $RMax^* = \frac{RMax}{D}$.

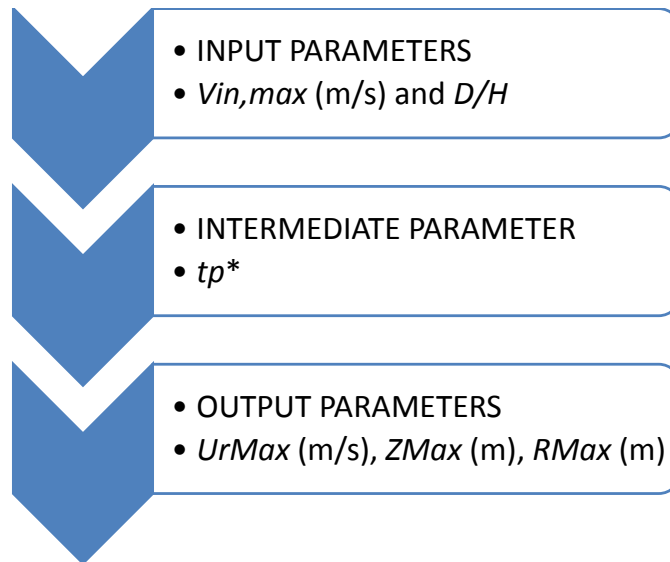


Figure 2.24: Parameters in the generalized procedure to simulate a downburst using the Paused Downburst model.

In order to simulate a downburst event with specified output parameters, $UrMax$, $ZMax$, and $RMax$, a wide range of combinations of the input

parameters, Vin, max and D/H , and of the intermediate parameter, tp^* , may be used. A large number of simulations were carried out for different input and intermediate parameters and a generalized model has been developed and is presented in the form of charts (refer to Figs. 2.25, 2.26, and 2.27). The following generalized procedure may be followed to simulate a downburst using the Paused Downburst model.

STEP 1: Select the required output parameters that characterize the downburst to be simulated—i.e., select values of interest for $UrMax$, $ZMax$, and $RMax$.

STEP 2: From CHART-ZT, select appropriate values of tp^* and of D/H corresponding to the desired $ZMax$ value.

STEP 3: Read off the value of $UrMax/Vin, max$ from CHART-UT corresponding to the selected values of tp^* and D/H from STEP 2. Hence, the required Vin, max value for the simulation can be computed.

STEP 4: Read off the value of $RMax/D$ from CHART-RT corresponding to the selected tp^* and D/H values from STEP 2. Hence, the required D value for the simulation; this also established the required value of H .

STEP 5: Establish the CFD computational domain (see Fig. 2.13) and carry out the desired simulation using the values of H , D , and Vin, max obtained from the steps above.

STEP 6: Extract the flow field data from the simulation at the paused time instant, $tp = (tp^* \times H)/Vin, max$. This extracted wind velocity data set

provide the time-independent Paused Downburst model output. Post-process the Paused Downburst model output to get the time-dependent output as described in Section 2.5.2 for use in any application such as for planned wind turbine loads analysis.

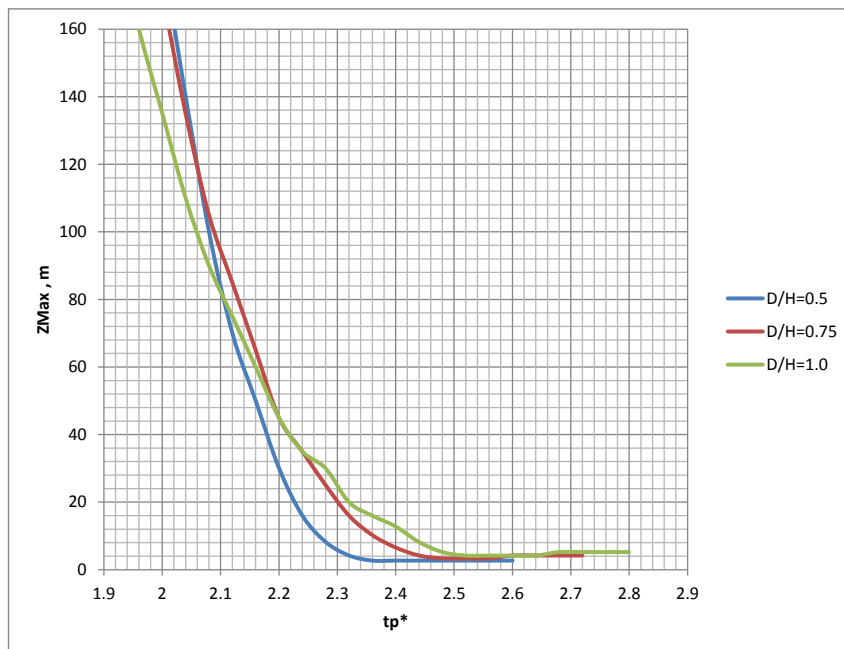


Figure 2.25: Variation of Z_{Max} with tp^* : CHART-ZT.

Although the charts presented in Figs. 2.25, 2.26, and 2.27 provide guidance for selection of model input parameters, it should be noted that small errors in the normalization might result. Hence, it is possible that when the CFD simulations are run, the time instant at which the simulation should be paused might not be exactly as suggested by the procedure. It is recommended that a few additional paused time instants are tried and the final data assessed

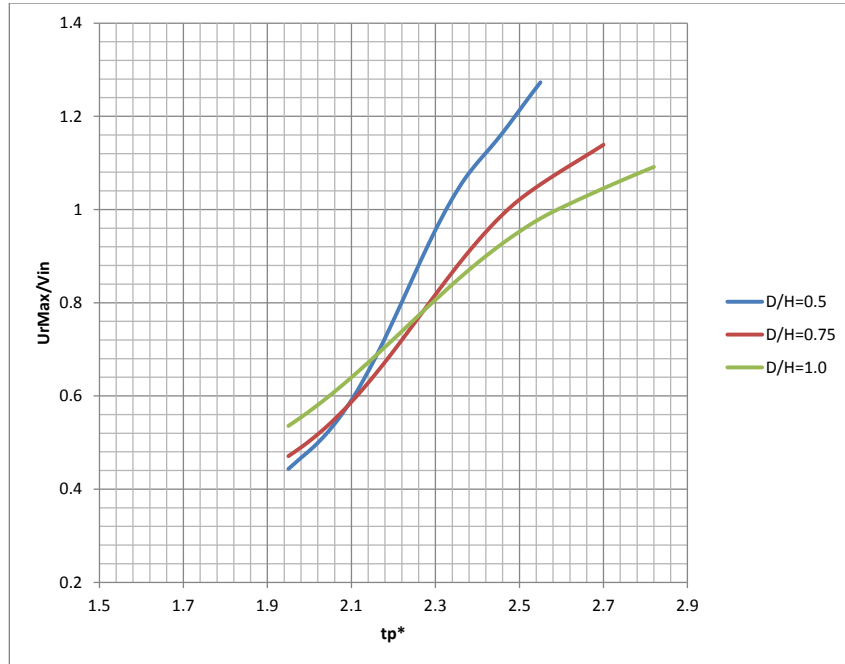


Figure 2.26: Variation of $UrMax$ with tp^* : CHART-UT.

so as to yield the desired output parameters. Results from the paused downburst should be subjected to the post-processing discussed in Section 2.5.2 to yield the full time-dependent downburst model output that could be used for any engineering application. A non-dimensional time of pause, tp^* , in the range from 2.1 to 2.5 is seen to best match actual downburst data. Values of tp^* below 2.1 are not advised; also, values of tp^* above 2.4 tend to cause maximum velocities very close to the ground (around 5 to 10m above ground) and these values are again not supported by actual observed data on downbursts. For the example case presented in Fig 2.15, the non-dimensional time

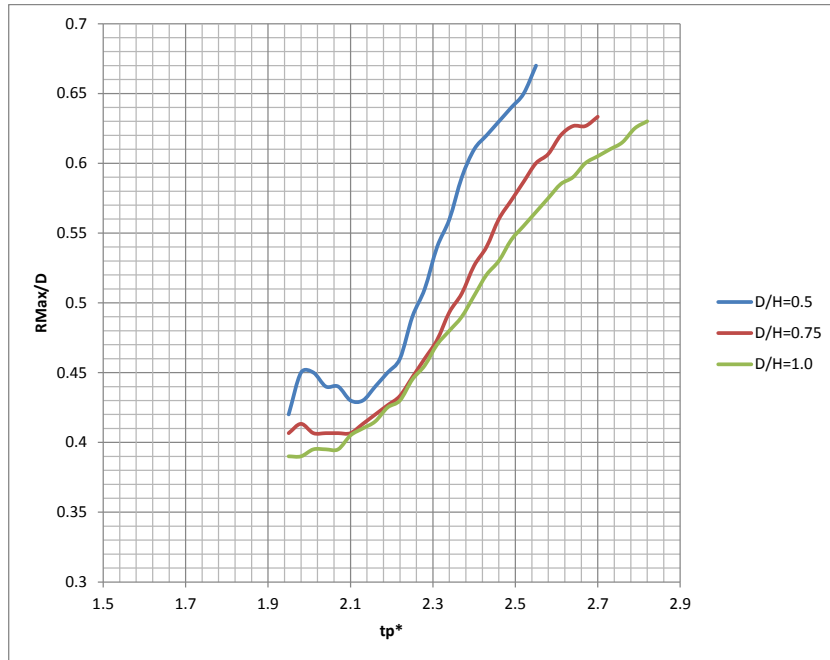


Figure 2.27: Variation of R_{Max} with tp^* : CHART-RT.

of pause, tp^* , is 2.14.

2.7 Summary

The basic computational fluid dynamics principles needed for describing the thunderstorm downburst phenomenon using the jet impingement concept were presented along with the mathematical formulation. A computational framework and domain needed for numerical solution of the problem using commercial CFD software were presented. The detailed procedure for development of the Paused Downburst model was presented where various issues

to be considered in the modeling of downbursts were identified and addressed logically in a step-wise manner. The model was validated and limitations identified. Finally, a generalized model for downburst simulation was presented that can be used for practical applications. Application of this model for wind turbine loads analysis is discussed next.

Chapter 3

Response of a wind turbine subjected to the simulated downburst winds

3.1 Introduction

In line with the objectives of this study, this chapter describes the development of the full flow field for wind turbine loads analysis and compares results with ongoing work where inflow wind fields for turbine loads analysis are based on alternative approaches not based on CFD. As described earlier, the full downburst wind field to which a wind turbine is subjected may be represented as a combination of turbulent and non-turbulent parts. The non-turbulent component of this wind flow field is obtained using the procedure presented in Chapter 2. In this chapter, we discuss the simulation of the turbulent component and the development of the combined (full) wind field. Details related to the wind turbine model used for the load studies are also presented here. After the wind field and the turbine model are established, the loads analysis procedure is described. Finally, results from the analysis with the CFD-based wind fields are compared with those obtained using alternative downburst-related wind fields as inflow to the turbine.

3.2 Wind field generation

3.2.1 Turbulence simulation

As discussed earlier, during a thunderstorm downburst, the wind velocity at any point in space may be understood as resulting from a mean (non-turbulent) component and a fluctuating turbulent component. The turbulent part of any of the three orthogonal wind velocity components is a zero-mean time series. Any single such time series can be generated from a target power spectral density (PSD) function. The PSD function (or power spectrum) used to generate the turbulence time series conveys information about the distribution of energy at different frequencies. Simulation of time series based on use of a power spectrum is described by Newland [15]. Given a target PSD for a specified point in 3-D space, a single turbulence component time series can be simulated using Inverse Fourier Transforms and Fourier amplitudes given in terms of PSD values. The simulation of turbulence time series at multiple points in space and for all three turbulence components at each point requires the use of target coherence functions in addition to target PSD functions. The coherence function, $Coh(x, y, f)$, between two random processes, x and y , is defined in terms of the individual power spectra, $S_{xx}(f)$ and $S_{yy}(f)$, and the cross power spectral density function, $S_{xy}(f)$, as follows:

$$S_{xy}(f) = Coh(x, y, f) \sqrt{S_{xx}(f)S_{yy}(f)} \quad (3.1)$$

Target coherence functions and target PSDs are used to generate cross power spectral density functions for all pairs of desired turbulence time series per

Eq. (3.1). The cross power spectra are then used to simulate the required turbulence time series at all points using the Fourier techniques. A detailed description of the procedure for simulating turbulence time series is described by Veers [22] and Hansen [6].

3.2.2 Wind field simulation using TurbSim

The procedure outlined in the previous section to simulate turbulent time series is implemented in the open-source software, TurbSim. This software was developed at the National Renewable Energy Laboratory (NREL). The user specifies spectral parameters and spatial configurations of interest—TurbSim allows one to define target turbulence PSD models, turbulence intensity levels, a wind profile, spatial grids, etc. Figure 3.1 shows how TurbSim transforms frequency-domain input generated wind flow field time series that are compatible with AeroDyn, which is used to compute aerodynamic loads on wind turbines.

In order to use flow field time series for wind turbine loads analysis, these time series need to be specified at discrete points in space on a two-dimensional grid (see Fig. 3.2) representing the rotor plane of the wind turbine. Simulated wind velocities on a single two-dimensional grid would be sufficient as long as the incident wind direction always remains normal to the rotor plane or the yaw error is small. A downburst flow field, as discussed, can be thought to result from a jet impingement on the ground. In addition, the flow is such that the inlet jet moves with time in a certain direction with the

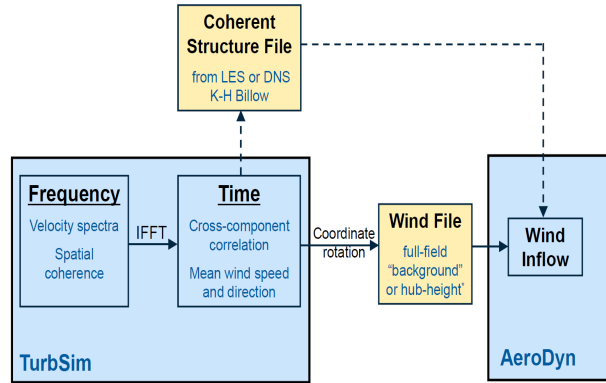


Figure 3.1: TurbSim simulation and its potential use in loads studies (Jonkman [8]). The coherent structures option is not employed in this study.

translational speed of the downburst. Hence, to a stationary observer (or to a wind turbine) in the vicinity of the downburst, the incident wind can change direction significantly during the downburst. In order to account for these large and sometimes rapid wind direction changes and associated yaw error, any wind turbine loads analysis is best carried out by subjecting the turbine to a flow field generated in a three-dimensional grid (or box) centered at the turbine hub.

In the present study, wind velocity time series were simulated at each point on a three-dimensional grid of $15 \times 15 \times 15$ points at 10 m spacing, centered at the turbine hub. All three orthogonal wind velocity time series

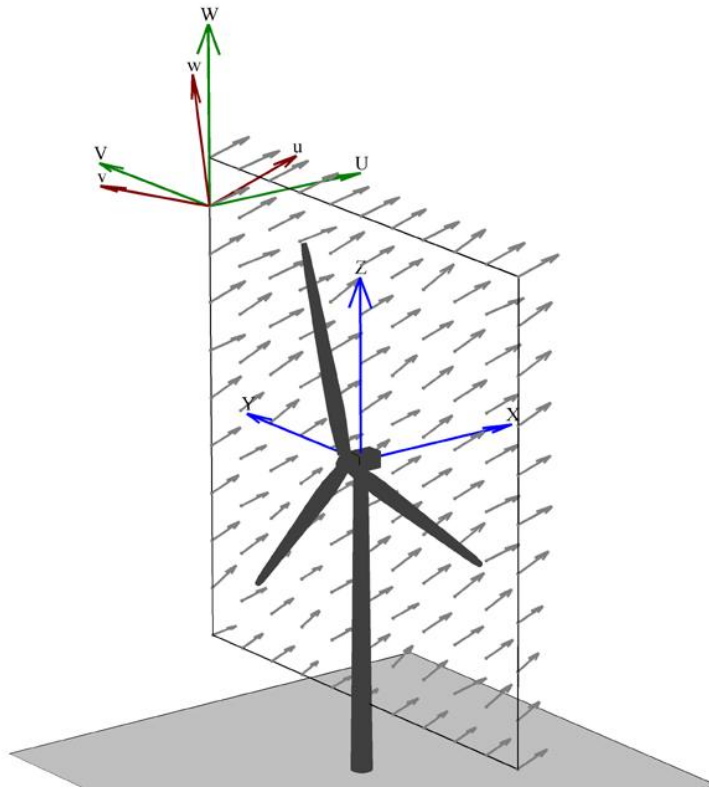


Figure 3.2: Flow field grid on the rotor plane of the wind turbine

were simulated by adding the turbulent component time series generated using the PSD and coherence functions to the non-turbulent component time series simulated using the Paused Downburst model. The radial and axial velocity components in cylindrical coordinates of the axisymmetric flow of the simulated downburst were transformed into the three-dimensional rectangular coordinate system at every point in the spatial grid centered at the turbine

hub. A user-defined FORTRAN subroutine was written and incorporated into AeroDyn to make use of the wind velocity time series in aerodynamic load computation. Additional information related to TurbSim and AeroDyn may be found in Jonkman [8] and Laino [12], respectively .

3.3 Wind Turbine Model

A utility-scale 5-MW wind turbine (the NREL 5-MW baseline wind turbine described in Jonkman et al. [9]) was used for the aeroelastic response analysis. A schematic diagram of the wind turbine and properties and dimensions of importance are presented in Fig. 3.3.

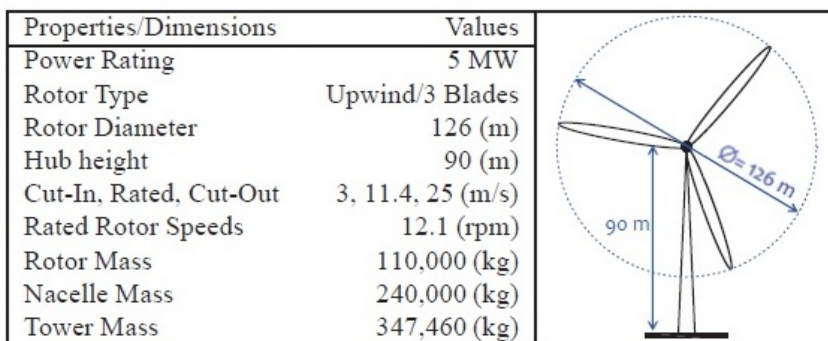


Figure 3.3: Wind Turbine Model Information (from Jonkman et al. [9]).

3.4 Wind Turbine Response analysis

After the flow field is simulated and the wind turbine model defined, another open-source program, FAST, is used to simulate the response of the model wind turbine subjected to the downburst-related flow field including turbulence. The program, FAST, was developed at NREL; it is a comprehensive aeroelastic simulator that may be used to predict extreme and fatigue loads on two- and three-bladed horizontal-axis wind turbines (HAWTs). The FAST user's guide (Jonkman and Buhl [10]) provides a detailed description of the files involved (input, output, etc.), the procedure to run the analysis, and other information.

3.5 Results and Discussion

Turbine loads analyses were carried out for two cases. Each case corresponds to a different set of downburst parameters, $UrMax$, $ZMax$, and $RMax$. Note that these are the output parameters of the Paused Downburst model discussed in Chapter 2. The input parameters needed to simulate the downbursts in order to obtain the target output parameters and the turbine loads analysis results are described next.

The parameters that describe the downburst include $UrMax$, $ZMax$, $RMax$, Krm , Td , U_{trans} , ϕ , R_o and U_{amb} ; the first three of these parameters have already been discussed. Among the other parameters, Krm is the rate of change of $Rmax$ with time; Td is the total duration of the storm; U_{trans} and ϕ are the translational speed and direction, respectively, of the downburst

with respect to the rotor plane (see Fig. 3.4); R_o is the initial position of the storm (touchdown point) relative to the turbine; and U_{amb} is the ambient wind speed assumed to act along the x direction as shown in Fig. 3.4. A value of θ_o (see Fig. 3.4) equal to π (radians) was used in the simulations. Table 3.1 provides details related to the CFD simulation and the input parameters for the Paused Downburst model (i.e., $V_{in, max}$, D , H and tp) used to obtain the target output parameters for the two cases studied. Table 3.2 provides details on all the storm parameters for the two cases.

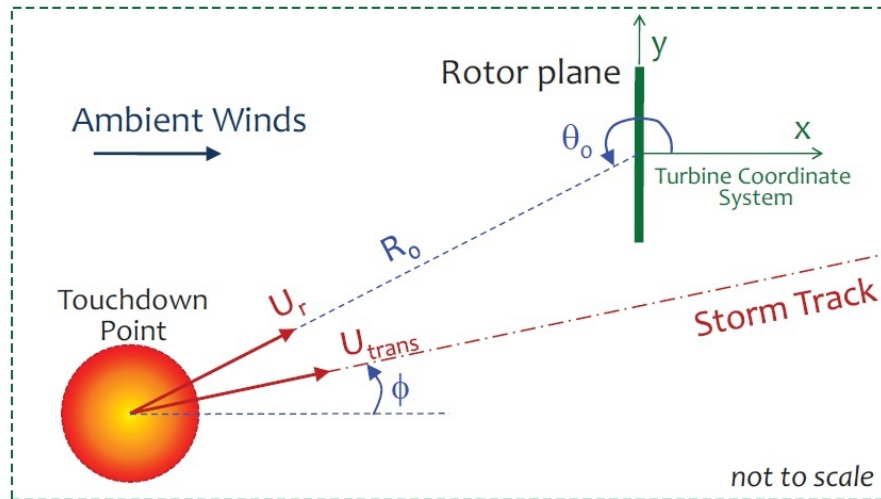


Figure 3.4: Plan view of the downburst and the wind turbine (taken from Nguyen et al. [16]).

The FAST program was used for the wind turbine loads analysis for the two cases. Results from using the Paused Downburst model to simulate the downbursts are compared to those obtained using the model of Nguyen

	$UrMax$ (m/s)	$ZMax$ (m)	$RMax$ (m)	H (m)	D (m)	Vin,max (m/s)	tp (s)	tp^*
<i>Case1</i>	26.4	60	430	2000	1000	40	107	2.14
<i>Case2</i>	22.16	40	860	2000	2000	30	148	2.22

Table 3.1: Values of the output and input parameters for the Paused Downburst model used for *Case1* and *Case2*.

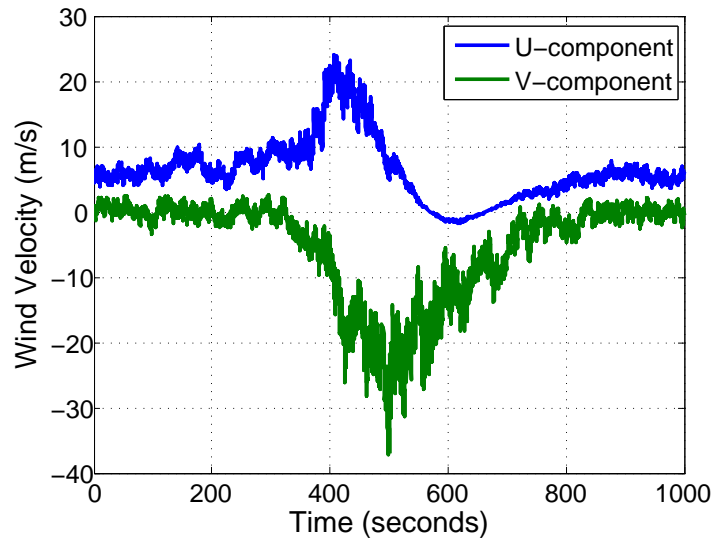
Krm (m/s)	Td (s)	U_{trans} (m/s)	ϕ (deg)	R_o (m)	U_{amb} (m/s)
1	960	8	15	4000	6

Table 3.2: Downburst parameters used in the wind turbine loads analysis (for both *Case1* and *Case2*).

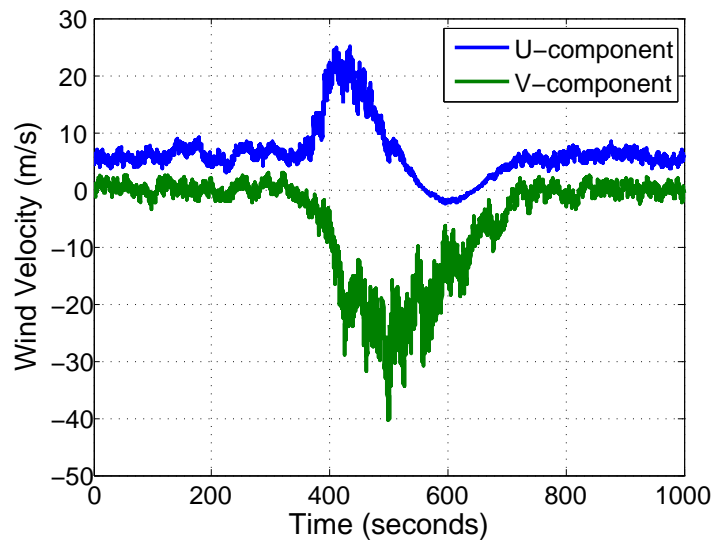
et al. [16], which is a slightly modified version of the model proposed by Vicroy [23]. Such comparisons are summarized in Figs. 3.5 to 3.12. The wind velocity plots (Figs 3.5, 3.7, 3.9 and 3.11) represent the wind speed at hub height (90 m). Simulations were run with and without the inclusion of turbulence. It is evident from the results that the Paused Downburst model are very similar to those obtained using the wind field model of Nguyen et al. [16]. The small kinks in Fig. 3.11 may be explained by the discontinuity in the normalized radial velocity profile at the radial position of the maximum radial velocity (Fig 2.19).

3.6 Summary

An application of the Paused Downburst model developed in Chapter 2 has been presented. Details of both the turbulent and non-turbulent components of the full wind field simulation were discussed. A procedure to stochastically simulate turbulent wind speed time series using power spectral

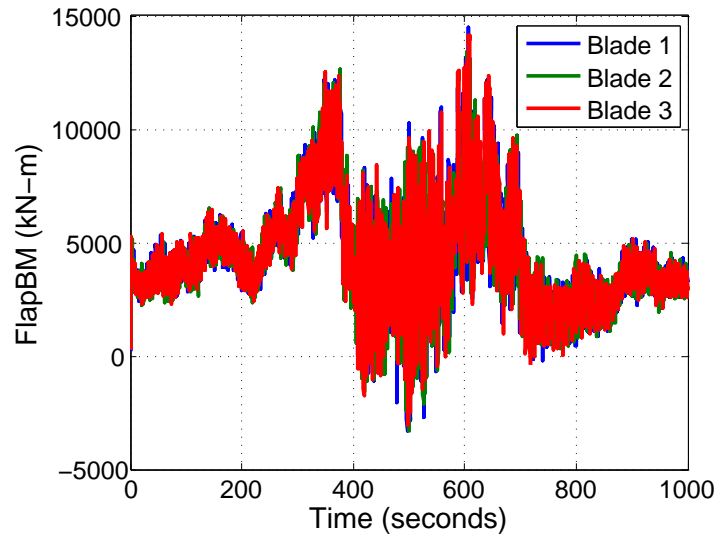


(a) Paused Downburst model.

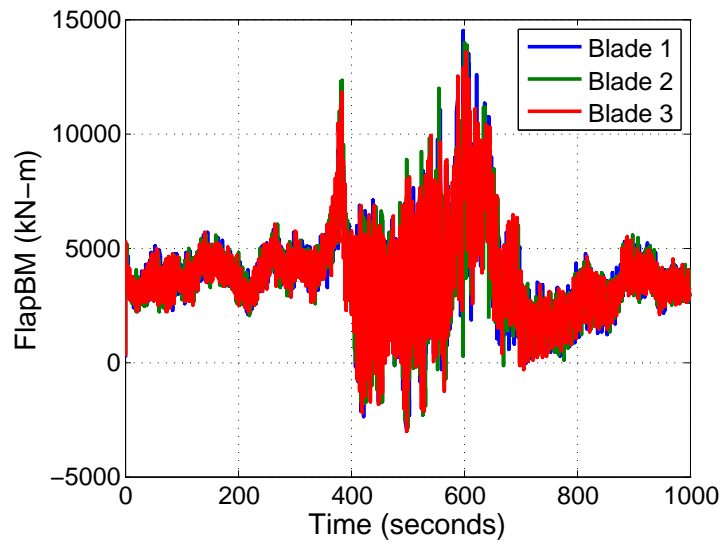


(b) Based on the model of Nguyen et al. [16]

Figure 3.5: Comparison of wind speed (with turbulence) at hub height for *Case1*.

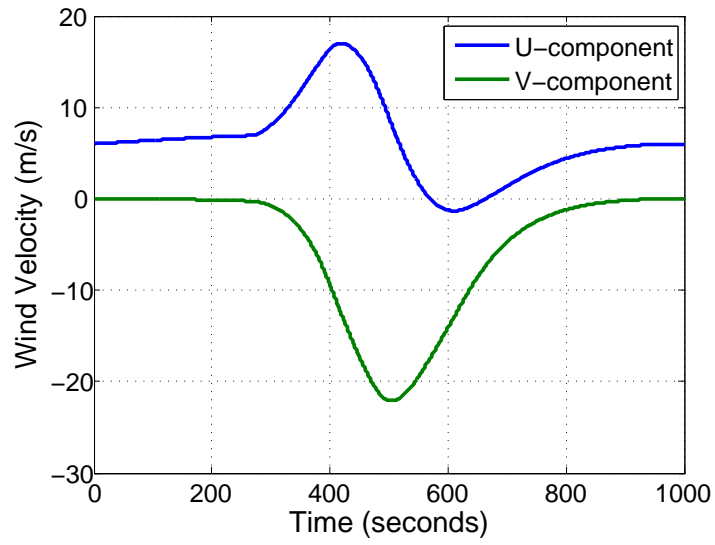


(a) Paused Downburst model.

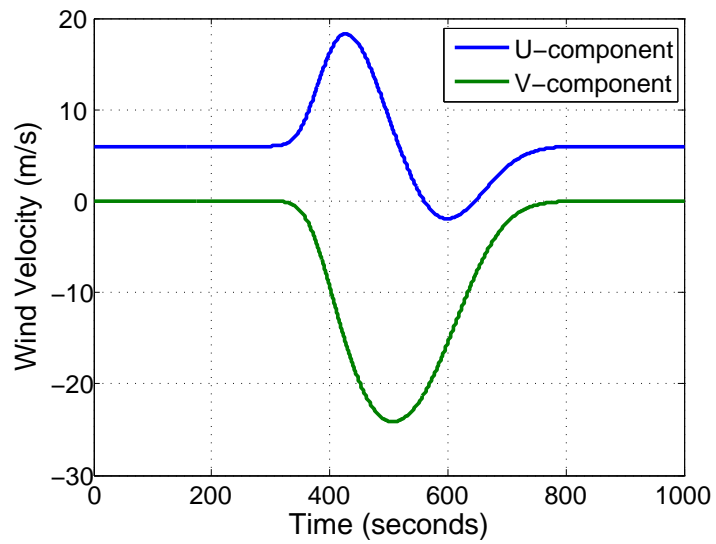


(b) Based on the model of Nguyen et al. [16]

Figure 3.6: Comparison of blade flap bending moment (with turbulence) for *Case1*.

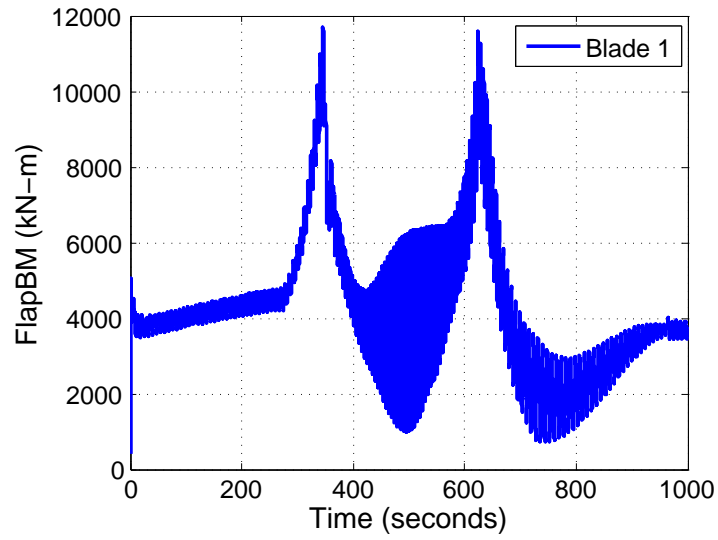


(a) Paused Downburst model.

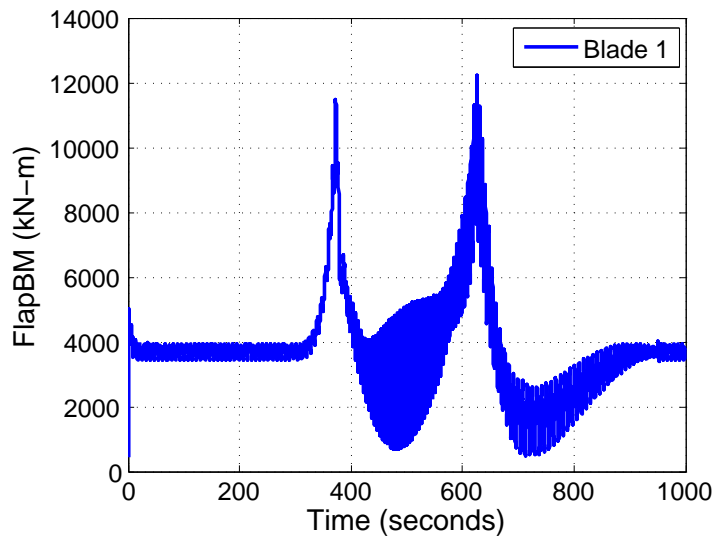


(b) Based on the model of Nguyen et al. [16]

Figure 3.7: Comparison of wind speed (without turbulence) at hub height for *Case1*.

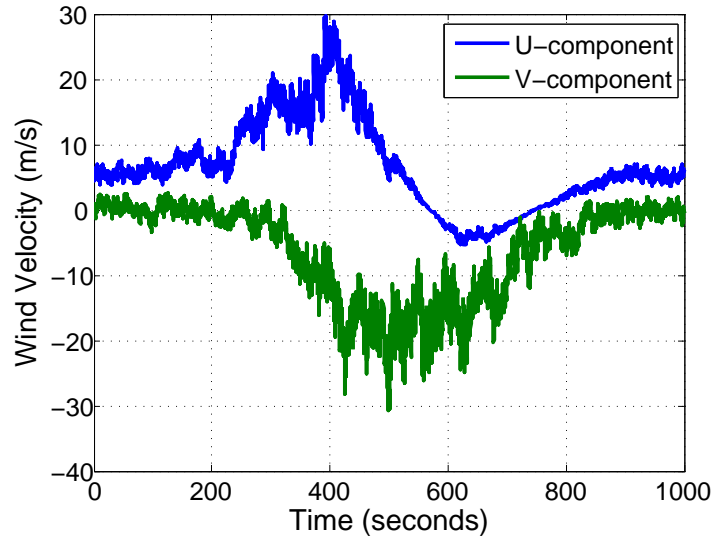


(a) Paused Downburst model.

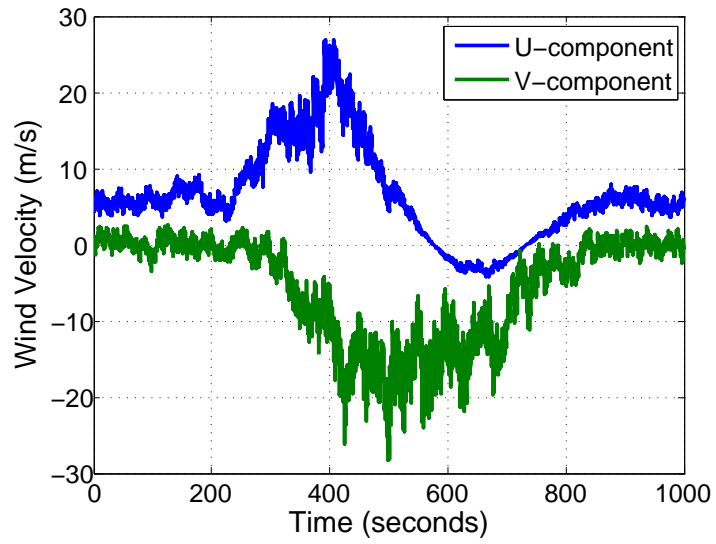


(b) Based on the model of Nguyen et al. [16]

Figure 3.8: Comparison of blade flap bending moment (without turbulence) for *Case1*

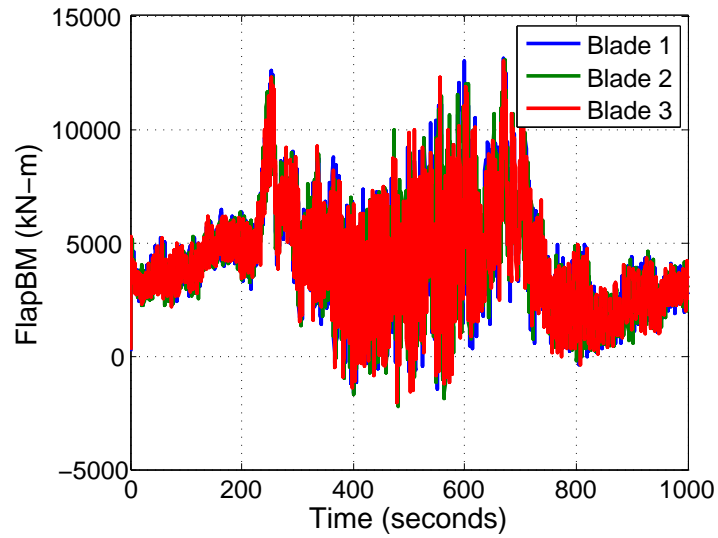


(a) Paused Downburst model.

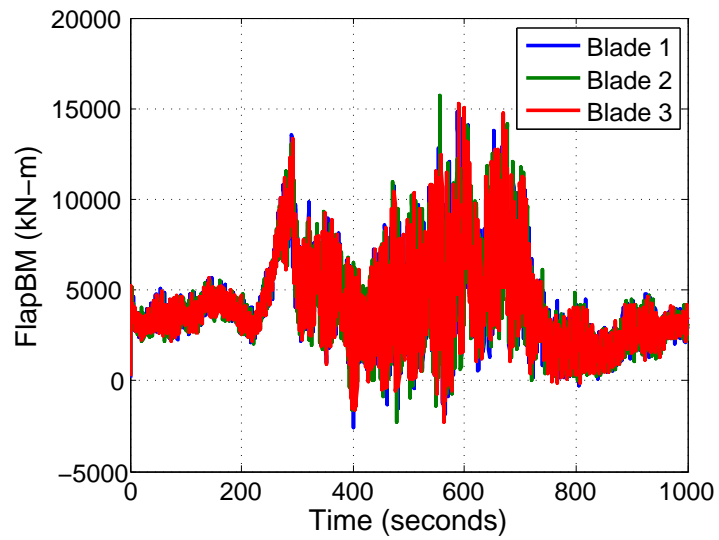


(b) Based on the model of Nguyen et al. [16]

Figure 3.9: Comparison of wind speed (with turbulence) at hub height for *Case2*.

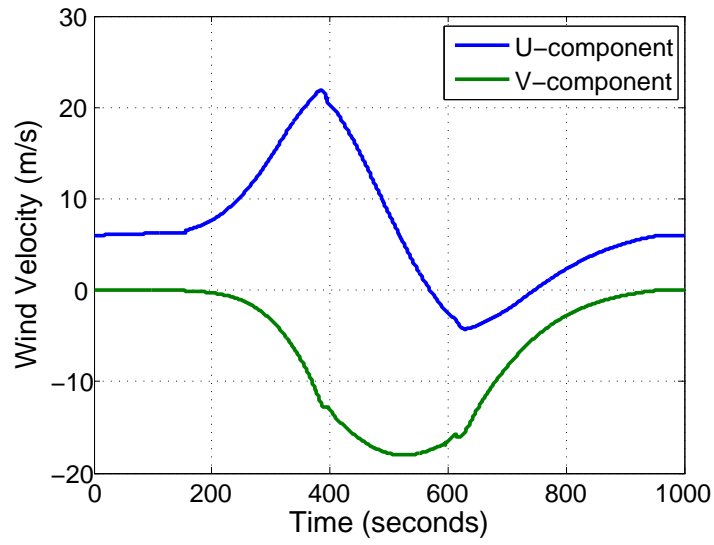


(a) Paused Downburst model.

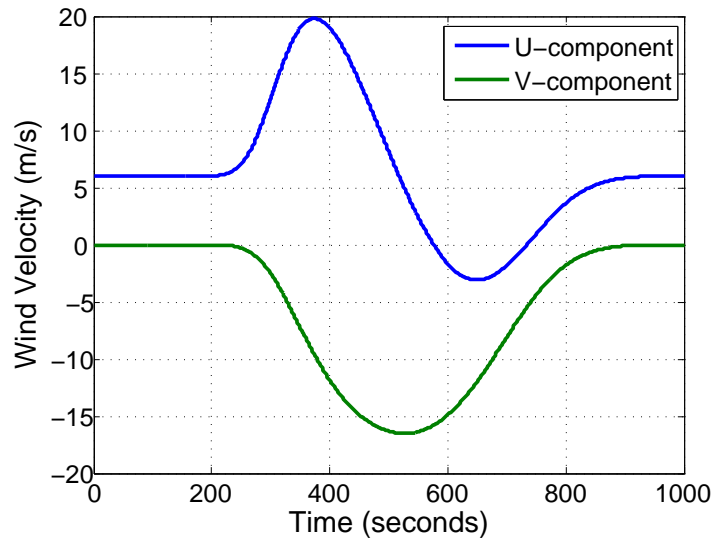


(b) Based on the model of Nguyen et al. [16]

Figure 3.10: Comparison of blade flap bending moment (with turbulence) for *Case2*.

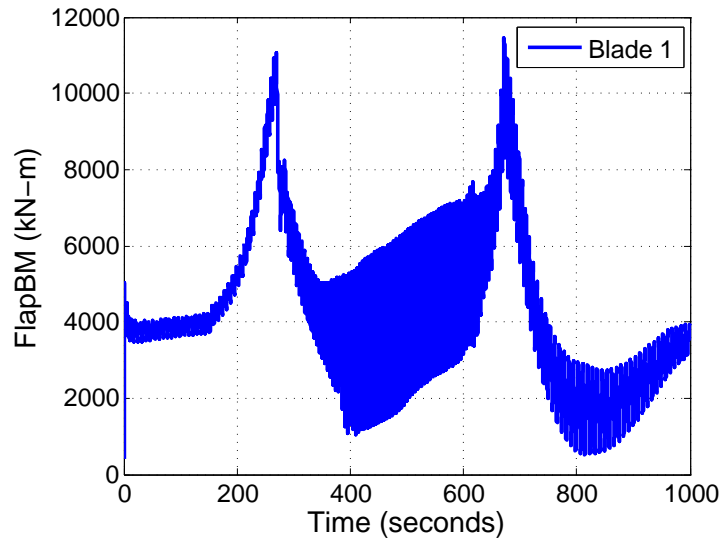


(a) Paused Downburst model.

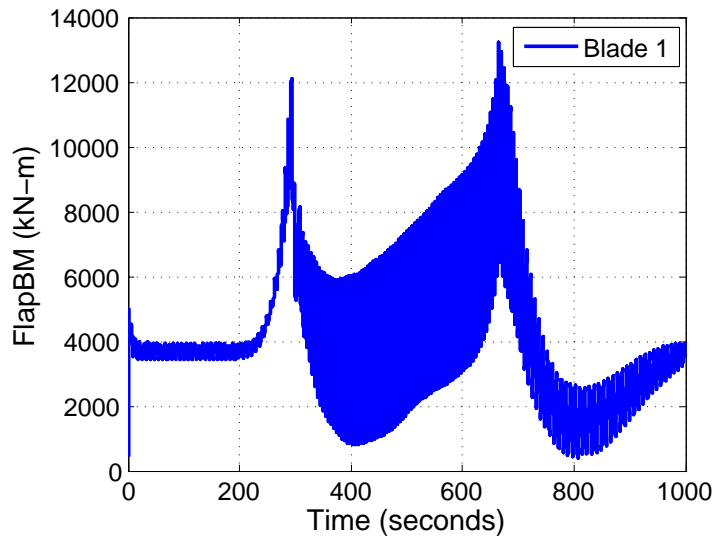


(b) Based on the model of Nguyen et al. [16]

Figure 3.11: Comparison of wind speed (without turbulence) at hub height for *Case2*.



(a) Paused Downburst model.



(b) Based on the model of Nguyen et al. [16]

Figure 3.12: Comparison of blade flap bending moment (without turbulence) for *Case2*.

and coherence functions was briefly described. Details related to the wind turbine model used in loads studies were presented. Loads analyses were carried out for two distinct downburst cases. The applicability of the Paused Downburst model was tested by comparing results with those based on an alternative model for downburst wind field simulation. Good agreement between the two approaches was observed for loads computed in both downburst cases. We conclude that the Paused Downburst model can serve as a viable computational model that may be used as an alternative to available analytical models for simulating thunderstorm downbursts.

Chapter 4

Conclusions

4.1 Overview of the research study

In many regions of the world, thunderstorm downbursts are frequently occurring natural phenomena. Also, they have been known to influence wind turbines and sometimes cause damage to them. A study of the influence of downbursts on wind turbines helps in assessing potential risks to the performance of wind turbines. Downbursts are complex atmospheric events to simulate for use in practical applications such as wind turbine loads analysis. Some experimental and analytical/empirical models have been developed in the last few decades informed greatly by field data. The present study aims at developing an alternative model to simulate thunderstorm downburst using computational fluid dynamics (CFD) with appropriate simplifying assumptions. We also seek to assess the applicability of the developed CFD model in wind turbine loads analysis and to compare it with other ongoing research on downburst effects on wind turbines.

4.2 Concluding remarks

A computational model termed a “Paused Downburst” has been developed. Comparison with other models for downburst wind field generation has shown that this Paused Downburst model can emulate the characteristics of other downburst models and can be effectively used as an alternative procedure to simulate downbursts entirely using computational methods. This model development was clearly objective-driven; we sought to establish a model that would capture characteristics of a recorded and well-documented downburst event in the literature (the Andrews AFB downburst). Given that the model was applied to carry out dynamic analyses of wind turbines, it is clear that the nature of the simulated time series would have a key influence on the results. Hence, emphasis was given to developing a model that could resemble a Andrews AFB downburst-type time series. It is to be noted that the Paused Downburst model can only simulate a time series similar to that of the Andrews AFB downburst, which is assumed to be representative of typical downbursts. The same limitation holds for available analytical/empirical models for downbursts. This limitation is mainly because of a lack of sufficient available good-quality data that describe characteristics of downbursts.

4.3 Recommendations for future work

Based on the procedures developed here, it is suggested that additional computational models be created based on the “Paused Downburst” concept to simulate downbursts with non-axisymmetric three-dimensional character-

istics. Also, three-dimensional translatory downbursts should be studied to reflect realistic downbursts. None of these models can be considered reliable unless they are validated using recorded downburst data. Hence, an extensive program to record downburst time series at various locations is recommended. This would help to understand realistic storm/downburst characteristics and, thus, could lead to the development of more accurate models to simulate downbursts for engineering applications such as in wind turbine loads studies.

Bibliography

- [1] A. Alahyari and E. K. Longmire. Dynamics of experimentally simulated microbursts. *American Institute of Aeronautics and Astronautics*, 33:2128–2136, 1995.
- [2] V. Anabor, U. Rizza, G. A. Degrazia, and E. de Lima Nascimento. Numerical modelling of microburst with large-eddy simulation. *Atmos. Chem. Phys. Discuss.*, 10, 2434524370, 2010.
- [3] M. T. Chay. Physical modeling of thunderstorm downbursts for wind engineering applications. Master’s thesis, Texas Tech University, 2001.
- [4] M. T. Chay, F. Albermani, and R. Wilson. Numerical and analytical simulation of downburst wind loads. *Engineering Structures*, 28:240–254, 2006.
- [5] T. T. Fujita. *The Downburst: Microburst and Macroburst*. SMRP, The University of Chicago, 1985.
- [6] M. O. L. Hansen. *Aerodynamics of Wind Turbines*. Earthscan, London, UK, 2008.
- [7] M. R. Hjelmfelt. Structure and life cycle of microburst outflows observed in colorado. *Journal of Applied Meteorology*, 27:900–927, 1988.

- [8] B. J. Jonkman. TurbSim User's Guide: Version 1.50. Technical report, National Renewable Energy Laboratory, Golden, Colorado, 2009.
- [9] J. M. Jonkman, S. Butterfield, W. Musial, and G. Scott. Definition of a 5-mw reference wind turbine for offshore system development. Technical report, National Renewable Energy Laboratory, Golden, Colorado, 2009.
- [10] J. M. Jonkman and M. L. Buhl Jr. FAST User's Guide. Technical report, National Renewable Energy Laboratory, Golden, Colorado, 2005.
- [11] J. Kim and H. Hangan. Numerical simulations of impinging jets with application to downbursts. *Journal of Wind Engineering and Industrial Aerodynamics*, 95:279–298, 2007.
- [12] D. J. Laino and A. C. Hansen. User's guide to the wind turbine aerodynamics computer software aerodyn. Technical report, Windward Engineering, LC, Salt Lake City, UT, 2002.
- [13] C. Li, Q. S. Li, Y. Q. Xiao, and J. P. Ou. Simulations of moving downbursts using cfd. In *The Seventh Asia-Pacific Conference on Wind Engineering*, Taipei, Taiwan, November 2009.
- [14] W. E. Lin, L. G. Orf, E. Savory, and C. Novacco. Proposed large-scale modelling of the transient features of a downburst outflow. *Wind and Structures*, 10:315–346, 2007.
- [15] D. E. Newland. *An Introduction to Random Vibrations and Spectral Analysis*. Longman Group Limited, London, 1975.

- [16] H. H. Nguyen, L. Manuel, and P. S. Veers. Simulation of inflow velocity fields and wind turbine loads during thunderstorm downbursts. In *51st AIAA/ASME/ASCE/AHS/ASC Structures, Structural Dynamics, and Materials Conference*, Orlando, Florida, April 2010.
- [17] R. M. Oseguera and R. L. Bowles. A simple, analytic 3-dimensional downburst model based on boundary layer stagnation flow. Technical report, NASA Langley Research Center, Hampton, VA, 1988.
- [18] W. Qu, B. Ji, and J. Wang. Numerical analysis of factors influencing the downburst wind profiles. In *The Seventh Asia-Pacific Conference on Wind Engineering*, Taipei, Taiwan, November 2009.
- [19] R. P. Selvam and J. D. Holmes. Numerical simulation of thunderstorm downdrafts. *Journal of Wind Engineering and Industrial Aerodynamics*, 41-44:2817–2825, 1992.
- [20] A. Sengupta, F. L. Haan, P. P. Sarkar, and V. Balaramudu. Transient loads on buildings in microburst and tornado winds. *Journal of Wind Engineering and Industrial Aerodynamics*, 96:2173–2187, 2008.
- [21] A. Sengupta and P. P. Sarkar. Physical and numerical modelling of thunderstorm downbursts. *Journal of Wind Engineering and Industrial Aerodynamics*, 96:345–365, 2008.
- [22] P. S. Veers. Three-dimensional wind simulation. Technical report, Sandia National Laboratories, Albuquerque, New Mexico and Livermore, Cal-

ifornia, 1988.

- [23] D. D. Vicroy. A simple, analytical, axisymmetric microburst model for downdraft estimation. Technical report, NASA Langley Research Center, Hampton, VA, 1991.
- [24] D. C. Wilcox. *Turbulence Modeling for CFD*. DCW Industries, Inc., La Cañada, California, 1993.
- [25] G. S. Wood, K. C. S. Kwok, N. A. Motteram, and D.F. Fletcher. Physical and numerical modelling of thunderstorm downbursts. *Journal of Wind Engineering and Industrial Aerodynamics*, 89:535–552, 2001.

Vita

Phanisri Pradeep Pratapa was born in Machilipatnam, Andhra Pradesh, India. His father, Mr. Pullaiah Pratapa works for the state government and his mother is Mrs. Padmavathi Pratapa. Pradeep got his undergraduate degree from the Indian Institute of Technology, Madras in July, 2010. He was accepted into the structural engineering graduate program at The University of Texas at Austin in Fall 2010.

Permanent address: F14, Lotus Legend Apts, Vidyadharapuram,
Vijayawada, Andhra Pradesh, INDIA.
PIN:520012

This thesis was typeset with L^AT_EX[†] by the author.

[†]L^AT_EX is a document preparation system developed by Leslie Lamport as a special version of Donald Knuth's T_EX Program.